Assembling an atomically defined molecular junction

Megan Cowie

Department of Physics
McGill University
Montréal, Québec
Canada
April 2018

A thesis submitted to McGill University
in partial fulfillment of the requirements for the degree of
Master of Science

TABLE OF CONTENTS

Chapters

LIST OF FIGURES

Figure

LIST OF TABLES

Table

ABSTRACT

The main challenge with studying single molecules at surfaces is that, in order to provide meaningful information about the mechanics of single-molecule transport, the exact atomic structure of the electrode-molecule junctions must be perfectly defined. In this thesis, I describe a approach for assembling an atomically defined Pt(110)-C60-W junction using a UHV STM/AFM/FIM system. This approach involves a combination of STM characterization of the bottom (Pt) electrode and FIM characterization of the top (W) electrode. In the final section of this thesis, I outline a novel method of determining the atomic tip coordinates from an experimental FIM image. This is the final piece of the puzzle necessary for the assembly of a C60 junction which has an atomically defined contact geometry. This powerful approach to studying single-molecule transport will enhance our understanding of charge flow at small dimensions, and will have immense value for the up-and-coming field of nanoelectronics by validating theoretical modelling approaches.

RÉSUMÉ

Le défi principal avec l'étude de l'électronique moléculaire sur les surfaces s'agit de définir la structure atomique exacte de l'électrode et de la molécule seule pour avoir de l'information significatif sur les mécaniques du transport. Dans ce thèse, je décris une approche pour avoir un jonction Pt(110)-C60-W défini l'atome en utilisant une système UHV STM/AFM/FIM. Cette approche implique une combinaison de la caractérisation STM de l'électrode inférieure (Pt) et de la caractérisation FIM de l'électrode supérieure (W). Dans la section ultime de cette thèse, je présente une nouvelle méthode pour déterminer des coordonnées de la pointe atomique à partir d'une image FIM expérimentale. C'est la dernière pièce du casse-tête nécessaire pour l'assemblage d'une jonction C60 qui a une géométrie de contact définie atomiquement. Cette approche puissante de l'étude du transport de molécules seules améliorera notre compréhension du flux de charge sur des petites dimensions et aura une immense valeur pour le domaine prometteur de la nanoélectronique en validant des approches de modélisation théorique.

ACKNOWLEDGEMENTS

I would like to thank my supervisor, Prof. Peter Grütter, for giving me the opportunity to work with a unique and impressive microscope: the ‘FIM System’, and for encouraging me to pursue my interests. I am extremely grateful for his guidance and enthusiasm.

My sincere thanks to Yoichi Miyahara for his expertise during each of the FIM System repairs. Without his assistance, I would not have known where to begin. His unlimited patience has helped me gain much more confidence with the inner workings of the FIM System.

Many thanks to Oscar Iglesias Freire for introducing me to the FIM System during the summer of 2016, when I first arrived at McGill. I appreciated his attention to detail and his passion for science immensely; it was a great pleasure to work with him.

Thank you to John Smeros for his assistance with maintaining the mechanical components of the FIM System, and to Robert Gagnon for his help with SEM imaging.

Additional thanks to the Grütter Group for engaging conversations and being such friendly faces in the lab. Finally, thank you Mom, Dad, and Allyson for your love and support.

AUTHOR CONTRIBUTIONS

The FIM System and general approach to create an atomically defined contact, described in Sections 2-4 of this thesis, were developed by the many former generations of FIM System operators. Oscar Iglesias Freire first implemented the use of Pt(110) samples, and consequently added the oxygen-cleaning step to the sample preparation procedure (Section 3). Oscar also helped acquire the STM image shown in Figure 3.4.

The tip model described in Section 5 of this thesis was developed by the author.

1 Introduction

In 1955, shortly after the advent of the transistor at Bell Labs, the first modern computer was born. It had 684 transistors, occupied 39.5 cubic feet, and weighed more than 1,000 pounds.[2] Every year since then, with every major advancement in nanofabrication technology, computers have become progressively smaller, cheaper, and more powerful. Today, most microprocessors contain billions of transistors with gates that are a mere 14 nm in length – that's less than 70 silicon atoms across.

If computer components are to continue to miniaturize, however, several challenges must be overcome. Firstly, at sub-10 nm device scales, quantum effects – such as quantum confinement and source-to-drain tunneling leakage – begin to compromise device performance.[3,4] Additionally, heightened sensitivity to the number and position of dopant atoms can introduce undesired variability between silicon chips.[4] Therefore, research is increasingly looking toward materials other than silicon, which can be more easily manufactured with the atomic precision necessary for sub-10 nm devices. In this regard, single molecules, which can be precisely designed and synthesized using the well-established prowess of synthetic chemistry, are a strong contender.

The concept of of using single molecules as circuit elements is not new, though it has garnered much interest in recent years, as we push our sights to sub-10 nm commercial technology. The field of molecular electronics dates back to 1974, when Aviram and Ratner first proposed that a single organic molecule could be used as a current rectifier.[5,6] The first groundbreaking experimental work measuring single molecule transport, accomplished by Tour and Reed in 1997, involved approaching two molecule-coated sharp electrodes together until the first onset of conductivity.[7] Today, a variety of sophisticated single-molecule devices have been created,[8,9] often employing tactics similar to Tour and Reed's inceptive experiment.

The next step toward single-molecule devices is to develop a comprehensive theoretical description of charge transport across the electrode-molecule-electrode junction. This brings about a major experimental challenge: In order to be able to reliably and accurately compare experimental results to theory, the position of *every* atom involved in the junction must be known, since variations in the contact geometry can lead to significant variations in conduction properties.[10, 11, 12]

In this thesis, I describe an approach to assemble an atomically defined single-molecule contact, using an ultra-high vacuum (UHV) scanning tunneling/ atomic force/ field ion microscope (STM/AFM/FIM) (Section 2). The bottom electrode of the single-molecule junction is a single Pt(110) crystal, which is atomically characterized using STM (Section 3). The top electrode is an electrochemically polished sharp tungsten tip (Section 4). In Section 5, I describe a new approach to determine the atomic coordinates of the sharp tungsten tip.

2 Ultra-high Vacuum System

My beginning months in the Grütter Group were spent learning how to operate and repair the 'FIM System': an ultra-high vacuum combined STM/AFM/FIM. The microscope, which is unique in the world, is entirely home-built: It has been designed, assembled, and improved by mainly students for the better part of three decades. The incorporation of FIM is what makes this system exceptional. In particular, it is highly promising for single-molecule transport experiments (see Section 1), since FIM allows for *in situ* characterization of the atomic configuration of the SPM tip.

The FIM system has three chambers: an airlock chamber, which is used for moving samples and tips in and out of vacuum; a preparation chamber, in which samples (Section 3.1) and tips (Section 4.1) are prepared for experiments; and a measurement chamber, where STM (Section 2.1), AFM, and FIM (Section 2.2) experiments take place.

2.1 Scanning Tunneling Microscopy

The scanning tunneling microscope (STM), invented by Gerd Binnig and Heinrich Rohrer in 1979,[13] relies on quantum mechanical electron tunneling between a sharp probe (tip) and a sample. In STM, the tip is brought very near to, but not in contact with, the sample surface. Due to the wave nature of electrons, there is a nonzero probability that they will cross the vacuum barrier between the tip and sample, provided the tip is sufficiently close to the surface.

In order to understand STM, it is necessary to understand tunneling, which is easily introduced by approximating the vacuum gap as a one-dimensional, finite, square potential barrier $U(z)$. Classically, the energy (E) of an electron in this potential is:

$$E = \frac{p^2}{2m} + U(z) \tag{2.1}$$

where m is the electron mass and p is its momentum. Outside the barrier(where E > U(z)), the classical momentum has a real, non-zero solution; however, inside the barrier (in regions where E < U(z)), there is no real solution for the momentum, meaning that penetration across the barrier is classically forbidden.

The quantum mechanical wavefunction of the electron is:

$$E\psi(z) = -\frac{\hbar^2}{2m}\frac{d^2}{dz^2}\psi(z) + U(z)\psi(z) \tag{2.2}$$

which, in the case of the rectangular potential barrier $U(z)$, has solutions:

$$\psi(z) = \psi(0)e^{\pm iz\frac{\sqrt{2m(E-U)}}{\hbar}} \tag{2.3}$$

In regions where E > U(z), the wavefunction takes the form $e^{\pm ikz}$, so the probability ($|\psi|^2$) of finding the electron inside the well is positive, and its momentum ($p = \hbar k$) is real and nonzero, as in the classical case. In regions where E < U(z), however, the wavefunction takes the form $e^{\mp \kappa z}$, which describes an exponential decay along $\hat{z}$. Therefore, unlike the classical case, the electron has a nonzero probability (which decays exponentially with distance) of penetrating the potential barrier.

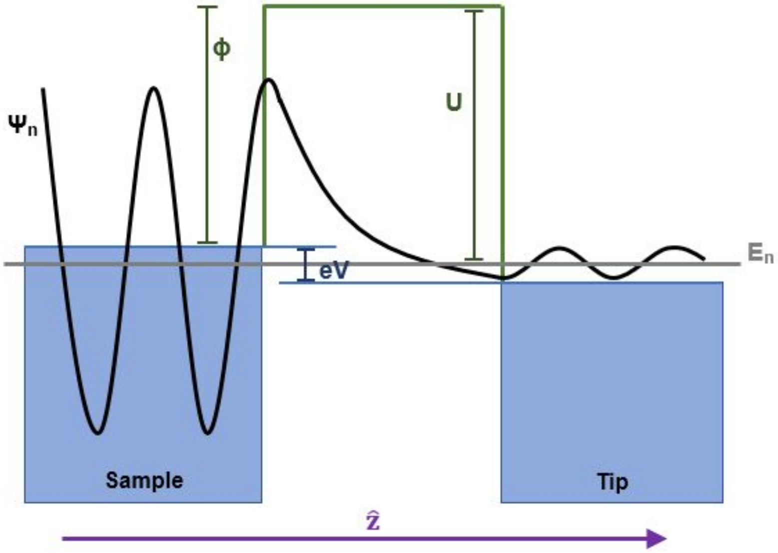

Figure 2.1: One-dimensional tunneling model: The wave function of an electron with energy E_n as it tunnels from the sample to the tip.

Figure 2.1 illustrates how this tunneling model gives a basic picture of the STM tip-sample junction. In the case of tunneling from the sample to the tip, the potential barrier height U is related to the sample work function ϕ, and the electron energy E_n corresponds to an occupied energy level in the sample. If the sample and tip work functions are equal, then the tunneling rates from the sample to the tip and vise versa are equal and opposite, so no net tunneling occurs. Therefore, a small bias V is applied between the tip and the sample. This unbalances the tunneling rates, so that tunneling is preferred in one direction.

The current measured in STM originates from the electrons that are successfully transmitted across the tunneling barrier. This current is proportional to the probability that electrons will tunnel through the barrier, $|\psi|^2$. Specifically,

$$I \propto \sum_{E_f - eV}^{E_f} |\psi_n(0)|^2 e^{-2\kappa z} \tag{2.4}$$

where E_f is the Fermi energy. The tunneling current, therefore, decreases exponentially with tip-sample separation distance, giving the STM remarkable sensitivity in the z-direction.

Finally, given that the local density of states (the number of states per energy level in some spatially localized region) for some energy interval ϵ is:

$$\rho = \frac{1}{\epsilon} \sum_{E-\epsilon}^{E} |\psi_n(z)|^2 \tag{2.5}$$

the tunneling current expressed in equation 2.4 can be expressed as:

$$I \propto V \rho e^{-2\kappa z} \tag{2.6}$$

Equation 2.6 is paramount for STM, since it shows that the *current is directly proportional to the local density of states*!

While the one-dimensional tunneling model is useful for introducing these basic characteristics of STM, it should be noted that it makes many gross oversimplifications. For instance, it does not account for the fact that there must be an accessible tip energy state in order for tunneling to occur. In more sophisticated tunneling models, these types of effects are accounted for. In the Bardeen tunneling model,[14] for example, tunneling only occurs when there is spatial overlap of the tip and sample wavefunctions, so it is necessary to know the density of states of both the tip and the sample. This point is the real motivation for the work outlined in Section 5 of this thesis, in which I describe an approach for finding the atomic coordinates of an experimental STM tip. To understand tunneling through any junction, including single molecules, the tip density of states, which is directly related to *tip structure*, must be known.

2.2 Field Ion Microscopy

The field ion microscope (FIM), invented Erwin W. Müller in 1951, was the first microscope to achieve atomic resolution.[15] It was a hugely influential technique in pioneering studies of adatom diffusion over solid surfaces,[16,15] grain boundaries and defects,[17,15] and, as in our case, the atomic structure of metal surfaces.[18,15] A typical FIM system has three main components: a multi-channel plate (MCP)[*], a phosphor screen[†], and high voltage power supplies. The MCP and phosphor screen are situated ∼10 cm away from the tip in a UHV chamber.

Operation of the FIM begins by backfilling the UHV chamber with an imaging gas, commonly He, to a pressure of 10^{-5} mbar by heating a quartz glass tube. A high negative bias (-1.1 kV) is applied to the MCP, and a high positive bias (4.0 kV) is applied to the screen. A positive bias is applied to the tip, producing an electric field in the tip vicinity. He atoms experiencing a sufficiently strong electric field (typically at tip voltages > 5 kV) become

---

[*] A MCP is a planar array of micron-scale electron multipliers. They are used to detect impinging radiation or particles (in our case, He^+) by producing an amplified, spatially resolved electronic signal. When an ion enters a channel on one side of the MCP, it hits a wall within the channel, which causes a cascade of electrons to be emitted from the channel wall. These electrons also, in turn, collide with the channel wall, which causes even more electrons to be emitted. This process repeats many times, and consequently, the signal (number of electrons) is amplified by many orders of magnitude by the time it reaches the opposite side of the MCP.

[†] A phosphor screen converts a spatially dispersed electronic signal into an optical signal by luminescence: The electron beams produced by the MCP excite electrons in the phosphor, which release photons as they decay back to their lower-energy states.

electrically polarized, and move to the tip by means of the electrostatic interaction between the positive tip and the negative induced He dipole. The He atoms then reach thermal equilibrium with the tip by 'hopping' over the surface[‡], and they continue to migrate over the tip until they are field ionized.

Field ionization, which can be loosely thought of as field emission in reverse,[19] is the ionization of gas-phase molecules in the presence of a strong electric field. In the absence of an electric field, the potential energy of an electron bound to an atom is a deep, symmetric trough. In the presence of a high electric field, the symmetry is broken, and the electron may tunnel into either free space or, if the atom is very close to a metal surface (and if the electron energy is at or above the Fermi level), into a metallic state.

Once field ionization occurs, the positive He ions accelerate toward the negatively charged MCP. The electrons that are emitted at the back of the MCP accelerate toward the positive phosphor screen and produce light, which is captured using a Nikon camera.

Atomic resolution in FIM arises from the fact that the electric field is enhanced at regions of high surface curvature, shown in the simple derivation below:

Consider two spheres of radius r_1 and r_2:

$$V_1 = \frac{kQ_1}{r_1}\ ,\ V_2 = \frac{kQ_2}{r_2}$$

$$Q = 4\pi r^2 \sigma$$

On a surface, $V_1 = V_2$:

$$r_1\sigma_1 = r_2\sigma_2$$

Given Gauss' Law, $E \propto \sigma$,

$$E \propto \frac{1}{r} \tag{2.7}$$

[‡] In general, the lateral component of the He atom velocity is a limiting factor for FIM resolution,[15] so tips are often cooled to low temperature prior to imaging. This results in energy transfer from the He atom to the tip, and drastically reduced lateral velocity. In my experience, however, cooling the tip is not necessary to achieve atomic resolution of the tip apex, perhaps due to the exceptional sharpness of our W tips.

In an emitter such as a W tip, the protruding atom sites at the tip apex have a much higher surface curvature than the emitter's shank, so the signal in FIM arises from the tip's protruding apex atoms. Contrast in a FIM image, similarly, is directly related to the spatial variation of the electric field. Since the electric field is most enhanced at protruding atom sites, a higher concentration of gas atoms will be locally attracted there, and in addition, the tunneling barrier width is reduced. Therefore, the brightest spots on the phosphor screen correspond to protruding atom locations.

At very high tip voltages (typically > 7.5 kV), atoms begin to be emitted from the tip surface, in a process known as field evaporation (or field desorption).[18,19] In the absence of an external electric field, the potential energy landscape of a metal and adsorbate takes approximately a Lennard-Jones shape. The potential energy landscape of the ionized metal and absorbate has a similar shape, but a higher energy globally, meaning that field evaporation is highly improbable. In the presence of an external field, however, the potential energy curves are distorted, meaning that there is a separation distance at which field evaporation becomes energetically favourable.

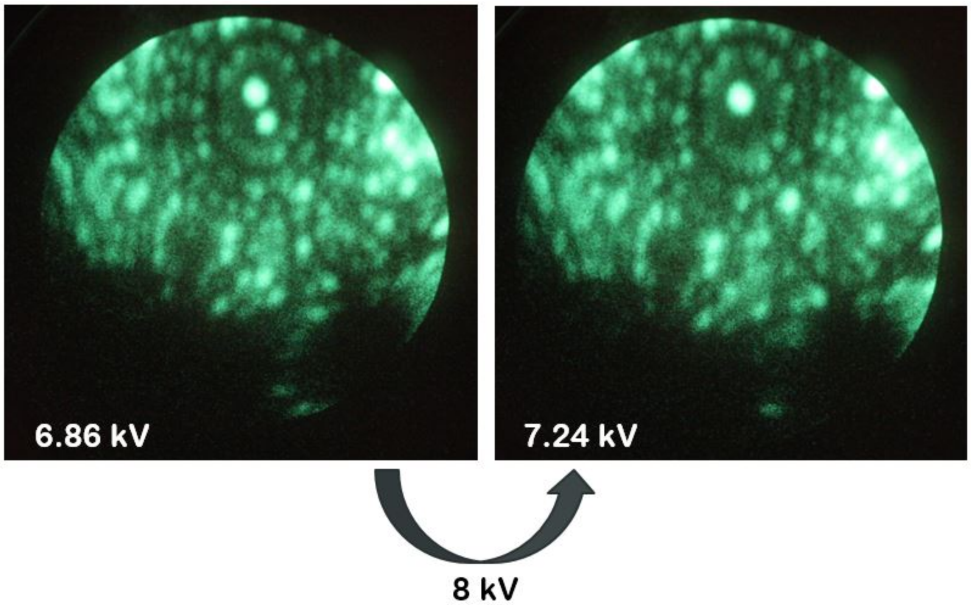

Figure 2.2: Field evaporation of a single apex atom. After the first image (L) was taken, the tip voltage was momentarily increased from 6.86 kV to roughly 8 kV, and then lowered back to 7.24 kV to take the second image (R).

For our purposes, the most useful application of field evaporation is to rid the tip of contaminants (adsorbate atoms will have a lower binding energy than lattice atoms, so will field evaporate first), and expose a pristine atomic layer. Within our lab, this procedure is often referred to as 'machining' the tip since, if due care is given, the tip shape may be controlled to some degree by varying the tip voltage. For example, Figure 2.2 shows a polycrystalline W tip before and after the controlled field evaporation of a single apex atom. This was accomplished by raising the tip voltage briefly from 6.86 kV (imaging voltage) to $\sim$ 8 kV (evaporation voltage), before returning to an imaging voltage of 7.24 kV.

2.3 Achieving Vacuum

Sometimes the FIM system can be challenging to work with, and much of that challenge arises from the fact the system is maintained under vacuum: the airlock chamber base pressure is $10^{-6} - 10^{-7}$ mbar, the preparation chamber pressure is in the low 10^{-9} mbar range, and the measurement chamber pressure is typically around 10^{-11} mbar.

What is the purpose of UHV in FIM system? Surface science experiments are commonly performed under vacuum for two main reasons: first, scattering interference during electron and ion beam experiments (such as Auger electron spectroscopy, Section 3.1.1) is reduced under vacuum; second, under vacuum, surfaces remain clean for longer periods of time. The vacuum conditions required to achieve these benefits are calculated below.

The mean free path (λ), which is the average distance a particle travels before it suffers a collision, is found using the kinetic theory of gases as:

$$\lambda = \frac{k_B T}{\sqrt{2}\pi d^2 P} \tag{2.8}$$

where d is the particle diameter and k_B, T, and P are the Boltzmann constant, temperature, and pressure. The incident flux, which is the number of particles hitting one side of a surface per unit time per unit area, is given by:

$$\Phi = \frac{nv}{4} \tag{2.9}$$

where n is the particle volume density and v is the average particle velocity. Assuming that every incident particle occupies a surface area of d^2, and assuming a 'sticking rate' of unity (i.e. every particle that hits the surface remains on the surface), the time to form a monolayer is:

$$t_{\mathrm{ML}} = \frac{1}{Fd^2} \tag{2.10}$$

A comparison of mean free path lengths and monolayer formation times at various pressures is shown in Table 2.1. This table shows that, in order to perform collision-free electron or ion beam experiments (i.e. when the mean free path is larger than the chamber dimensions), medium-high vacuum conditions are suitable. However, in order to to maintain a clean surface (i.e. when the time to form a monolayer is longer than the experiment time), ultra-high vacuum conditions are necessary. In the FIM system, base pressure in the measurement chamber is typically in the mid-low 10^{-11} mbar range, which means that the window in which the sample and tip surfaces are mostly 'clean' is on the order of three hours.

	Pressure (mbar)	Mean Free Path (m)	Monolayer Formation Time (s)
Atmospheric	10^3	10^{-8}	10^{-9}
Low (Rough)	1	10^{-5}	10^{-6}
Medium	10^{-3}	10^{-2}	10^{-3}
High	10^{-6}	10	1
Ultra-High	$< 10^{-10}$	10^5	10^4

Table 2.1: The mean free path length and monolayer formation time of an arbitrary particle of diameter 1 Å and molecular mass 10 g/mol, at various pressures at room temperature.

Many types of pumps are used to achieve vacuum, and different combinations of pumps must be used to achieve different vacuum levels. In the FIM system, the most relevant pumps are transfer pumps (Section 2.3.1) and entrapment pumps (Section 2.3.2).

2.3.1 Transfer Pumps

Transfer pumps remove air from a vacuum chamber by moving molecules from one side of the pump to the other. They are the most common type of pump, used to achieve anywhere from low (1 mbar) to high (10^{-8} mbar) vacuum. Two types of transfer pumps are used in the FIM system: turbomolecular pumps and rotary vane pumps.

Turbomolecular pumps create a pressure difference between the ‘front’ (i.e. section closest to the vacuum chamber) and ‘back’ of the pump by transferring momentum to gas molecules in the direction away from the vacuum chamber. Rotating at speeds of approximately 1000 rpm, these pumps consist of a series of fans. When a molecule comes into contact with an angled fan blade, mechanical energy is transferred to the gas molecule, resulting in an increase in momentum preferentially along the pump direction. This process (the molecule hits a fan and is ejected on the opposite side with additional kinetic energy) repeats for the entire pump length. Consequently, the gas is compressed, resulting in large pressure differences between the front and back of the pump. The pressure at the front of the FIM system’s Leybold Turbovac 340M magnetically levitated turbo pump, for example, is usually on the order of 10^{-11} mbar, while the pressure at the back of the pump is on the order of 10^{-3} mbar.

A ‘roughing pump’, or medium-low vacuum range pump, is necessary to evacuate the gas produced at the back of a turbomolecular pump. In the FIM system, rotary vane pumps are used for this purpose. Gas enters the pump through an inlet pipe that leads to a large circular cavity containing a rotating rotor and vanes. Once gas enters the cavity, the vanes – sealed with oil – close off both the inlet and outlet pipes. As the rotor rotates, the volume of the cavity decreases, resulting in gas compression. Finally, the vanes allow access to the outlet pipe, and the compressed gas is released into atmosphere.

2.3.2 Entrapment Pumps

Entrapment pumps remove gaseous species by trapping them in the solid state. In addition to their powerful pumping capabilities (they are necessary to push the vacuum limit to the UHV range), entrapment pumps are notably beneficial because they do not contribute to system vibrations. Another major benefit of entrapment pumps is that they are very effective for removing $\mathrm{H_2}$ (g), which is difficult for transfer pumps to remove due to its small size. The FIM system has three types of entrapment pumps: titanium sublimation pumps (TSPs), non-evaporable getter pumps (NEGs), and ion pumps and gauges.

TSPs are simple pumps, requiring only a titanium filament and a current source. When current (50 A) is applied through the titanium filament for a short amount of time ($\sim$ 1 minute), a very small amount of titanium sublimates inside the vacuum chamber and deposits on the chamber walls. Titanium is a reactive material which, when it combines with residual gas species, forms stable, solid products. For example, the reactions between solid titanium and three common residual gas species (O_2, N_2, and H_2O) are shown below:

$$Ti(s) + O_2(g) \rightarrow TiO_2(s)$$

$$2Ti(s) + N_2(g) \rightarrow 2TiN(s)$$

$$Ti(s) + 2H_2O(g) \rightarrow TiO_2(s) + 2H_2(g)$$

In addition, titanium readily physisorbs $\mathrm{H_2}$ (g) at room temperature. By trapping molecules in the solid state, TSPs effectively remove gaseous species from the environment, reducing the pressure within the vacuum chamber.

NEG pumps contain a solid, reactive ‘getter’ alloy which physisorbs residual gas species. Occasionally, the NEG pump must be heated to encourage absorbed material to diffuse deeper within the pump, so that new molecules may continue to be captured at the pump surface.

Ion pumps ionize residual gas species, and capture the ions at a solid surface within the pump. Electrons emitted at the pump cathode move under the presence of a magnetic field in helical trajectories toward the anode. Along the way, they may collide with – and ionize – gaseous species within the pump. The positively charged ions then accelerate toward the titanium cathode. Ion collisions cause titanium to be sputtered onto the walls of the pump and, like a TSP, this causes chemisorption and physisorption of gaseous species into the solid state. The amount of titanium sputtered is directly related to the vacuum pressure, so the higher the pressure, the faster the ion pump pumps.

Ion gauges are similar to ion pumps, in that they also remove gaseous species from the vacuum environment by ionizing and collecting them within the gauge. In addition to pumping, however, ion gauges give an indication of the pressure within the chamber by measuring the current that is generated at the cathode. (Current and pressure are linearly related.) These types of gauges are considered to be highly accurate in HV and UHV conditions.

2.3.3 Chamber Bakeout

Whenever the chamber is exposed to atmosphere (which is usually necessary to perform repairs), the interior of the chamber becomes coated with water and other contaminants. Once the chamber is sealed, these contaminants slowly desorb from the chamber walls, increasing the vapor pressure and making UHV unachievable. The desorption rate[20] of contaminants from a chamber wall Q_{des} is:

$$Q_{des} = Aq_{des}\frac{t_o}{t} \tag{2.11}$$

where q_{des} is the desorption flow density per unit area, A is the chamber wall area, t_o is a time constant, and t is the pumping time. This equation may be combined with Equation 2.12[20] to find the time needed to achieve some base pressure P_{base}:

$$P_{base} = \frac{Q_{des}}{S_{pump}} \tag{2.12}$$

$$P_{base} = \frac{A q_{des} t_o}{S_{pump} t} \tag{2.13}$$

where S_{pump} is the pumping speed. The pumping speed of the FIM system's Leybold Turbovac 340M magnetically levitated turbo pump is 270 L/s. Assuming q_{des} to be the desorption rate of stainless steel per unit area[20] ($2.7 * 10^{-4}$ Pa L s^{-1} m^{-2}), A to be 1 m^2, and t_o to be 1 hour, it would take 1000 hours to pump the chamber to 10^{-11} mbar!

Therefore, in order to reduce this pumping time, the chamber is 'baked', or heated to 80°C-120°C. This accelerates the pumping process by rapidly evaporating contaminants from the chamber walls. The bakeout typically takes several days, and care is taken to increase the temperature of the entire chamber at a similar rate and to a similar value, to prevent uneven thermal expansion between components.

3 Sample Preparation

Our proposed single-molecule junction is composed of a Pt(110) substrate, a C60 molecule, and an STM tip. In this section, I describe the procedures that are used to prepare the Pt(110) surface and deposit C60 molecules, and I show a preliminary characterization of the Pt(110) surface.

3.1 Pt(110) Surface Preparation

The Pt(110) sample is prepared in cycles of sputtering, annealing, and O_2 exposure. Sputtering is a widely used technique for the removal of contaminants from solid surfaces. The sputtering process has three steps. First, argon, which is an inert noble gas that does not chemically react with the sample, is introduced into vacuum to a partial pressure of 10^{-5} mbar. Then, an electron beam ionizes the argon atoms, and a negative sample bias accelerates the positive argon ions toward the sample. Finally, when the ions collide with the surface, their momentum transfer causes contaminants to be ejected from the sample.

The sputtering process, while effective for removing unwanted surface contaminants, is also highly disruptive to the crystal surface. Since the precise amount and location of material removed during sputtering cannot be controlled, sputtering roughens the surface by creating undesirable crystalline defects. Therefore, post-sputtering, the sample is annealed to improve the quality of the crystal surface. An atom's ability to move over a surface depends on the amount of energy it has and on its energy landscape. In general, surface atoms settle at sites that minimize their local potential energy. However, if the sample is heated, the surface atoms are able to overcome local energy barriers and diffuse. This effect is described by:

$$\Gamma = ve^{\frac{(-E_{diff})}{(k_B T)}} \tag{3.1}$$

where Γ is the hopping rate, v is the attempt frequency constant, E_{diff} is the potential energy barrier imposed by the energy landscape, and T is the temperature. In other words, as the thermal energy increases, the surface atom mobility increases. When the sample cools, the atoms will preferentially settle in their most stable configuration (the lowest energy well). By similar reasoning, annealing also causes contaminants within the crystal bulk to diffuse to the surface, where they can be removed in a subsequent sputtering cycle.

Given that carbon is a common contaminant of platinum, for cleaning platinum we have added an additional step to our standard sample cleaning procedure: introducing O_2 at a pressure of 10^{-7} mbar for 5 minutes as the sample is cooled. O_2 is highly chemically reactive with carbon, and so is extremely effective for the removal of carbon contaminants. The products of this reaction, CO and CO_2, being gases at room temperature, effectively carry the carbon away from the sample surface.

During the sputtering, annealing, and O_2 exposure cycles, a residual gas analyzer (RGA) is used to monitor the atomic and molecular species present in our preparation chamber under UHV. An RGA is a type of mass spectrometer: that is, the masses of the residual gas molecules are compared to known molecular masses to determine the residual gas molecular species. As gas molecules enter the RGA, they pass through an electron-emitting tungsten filament and are ionized. The ions then accelerate to a quadrupole mass analyzer. The quadrupole mass analyzer filters all species that do not have a particular mass-charge ratio (selected to correspond with known molecular species). The species that do pass through the quadrupole mass analyzer are collected to produce an electronic signal by means of an electron multiplier. The more molecules that pass through the filter, the larger the signal will be. The particular mass-charge ratio that is filtered can be adjusted to test for various molecular species.

3.1.1 Auger Electron Spectroscopy

Once the sample has undergone several sputtering cycles, it is characterized using Auger electron spectroscopy (AES). AES measures the elemental composition of a solid sample surface. In AES, the sample surface is bombarded with high-energy electrons (in our case, a 3 keV electron beam, which is generated by applying a 2.95 A current through a tungsten filament). These high-energy electrons generate holes in the atomic core energy levels in the sample. Higher-energy electrons then transition within the inner-shell to fill the lower-energy hole, and in doing so emit a photon that has energy equal to the difference between the two levels. The photon is absorbed by a second (valence) electron which, given this extra energy, overcomes its binding energy and is ejected from the atom. These emitted electrons – Auger electrons – are collected by a detector, by sweeping the detection energy over a range of interest (in our case, from 0-500 eV).

In practice, electrons' kinetic energy becomes dispersed by secondary effects such as scattering, leading to a huge inelastic electron background. Therefore, peaks in the number of Auger electrons collected by the detector as a function of energy, N(E), are difficult to discern from the background signal. Lock-in amplification is a particularly useful technique to overcome this low signal to noise ratio. With a lock-in, the energy that the detector measures is modulated about each DC value in the energy sweep. The combined lock-in and detector thus measures the derivative of the number of electrons emitted as a function of energy, dN(E)/dE, giving much sharper emission peaks.

Given that the Auger electrons' kinetic energy directly depends on the core electron energy levels, all elements give a unique characteristic Auger spectrum. By comparing measured Auger spectra against known spectra corresponding to each element, the elemental composition of the sample surface is determined. An important note is that AES is strictly a surface characterization, since electrons emitted from below the sample surface will lose kinetic energy to scattering reactions as they move through the bulk. Eventually, on the order of a few nanometers deep into the material, so much energy is lost to scattering events that the electrons are entirely unable to escape into vacuum and be detected.

A typical AES spectrum of a Pt(110) surface is shown in Figure 3.1.1. The left-most peaks correspond to known platinum peaks at 46 and 64 eV, and the centre peak corresponds to a carbon peak at 272 eV. The presence of the strong carbon peak indicates that the surface is carbon-contaminated. Therefore, before molecule deposition, additional sputtering cycles should be done on this sample until there is a significant diminishment in the carbon peak.

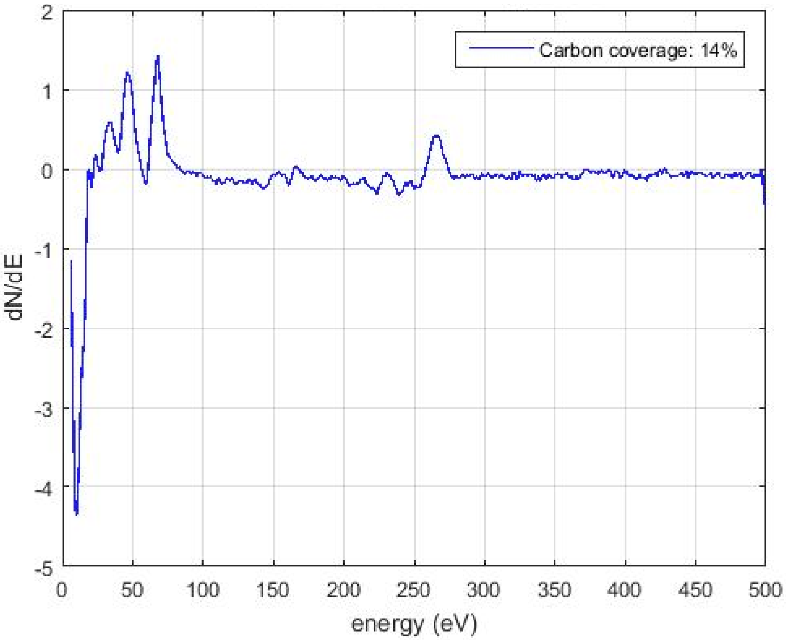

Figure 3.3: AES spectrum of a Pt(110) surface after two sputtering cycles. The left peaks correspond to platinum peaks at 46 and 64 eV, and the centre peak corresponds to a carbon peak at 272 eV.

3.1.2 Molecule Deposition

An Omicron EFM-3T e-beam evaporator is used to deposit C60 molecules on a clean Pt(110) surface. The evaporator has three main components: a crucible packed with C60, a tungsten filament, and a collimator. When current is applied to the filament, electrons are ejected and accelerate towards the crucible, which is biased to +180 V. Transfer of momentum from the electrons causes the C60 molecules to be ejected from the crucible. The collimator then focuses the C60 molecules in the direction of the sample, where they adsorb to the surface. An ammeter connected to the collimator is used to track the evaporation process: before evaporation begins, the flux through the collimator is strictly due to electrons emitted at the filament, so it is negative. As the current supplied to the filament is increased, causing more electrons to be emitted, the flux through the collimator becomes even more negative. Eventually, (typically at an applied current of 1.45 A through the filament) the current measured at the collimator becomes positive. This is the signature that evaporation has begun: now, contaminants and C60, which contribute positive flux, bombard the collimator (in addition to stray electrons from the filament). A flux of 3 mA through the collimator is maintained for 5 minutes, to deposit C60 on the Pt(110) surface at a density appropriate for single-molecule studies.

3.2 STM Characterization

The material that is used for the bottom electrode of the substrate-C60-tip single-molecule junction must meet two main criteria. First, it must be a metallic single crystal, since metallic single crystals are well-ordered, and their tunneling characteristics are generally well-understood. Second, the substrate must limit self-diffusion and diffusion of C60 molecules at room temperature, since diffusion contaminates the junction and the tip.

Diffusion of particles over a surface, which was previously described in Equation 3.1, depends on the potential energy barrier imposed by the landscape, E_{diff}. At a constant temperature, the higher the barrier, the less diffusion occurs. Therefore, for the bottom electrode, it is necessary to select a material that has a high diffusion barrier.

	$\boldsymbol{E_{diff}}$ (eV)		
	(100)	(111)	(110)
Ag	0.52	0.10	0.59
Al	0.60	0.13	0.60
Au	0.64	0.12	0.86
Cu	0.59	0.11	0.76
Ir	1.23	0.23	1.48
Ni	0.75	0.14	0.86
Pd	0.60	0.14	0.72
Pt	1.02	0.20	**1.21**
Rh	1.02	0.21	1.20

Table 3.1: Activation energy values for various metals, for various crystallographic planes: (100), (111), and (110). Values from Agrawal *et al.* (2002).[1]

Table 3.1 shows the activation energy values of various crystallographic planes of various metals. From this table, it is clear that many common metallic surfaces, such as Au(111) and Cu(100), are not optimal choices because they have a low activation energy. The Pt(110) surface was selected for the bottom electrode material because its activation energy is comparatively high at 1.21 eV.

An STM image of a C60-decorated Pt(110) surface is shown in Figure 3.4. The bright dots correspond to C60 molecules, and the vertical lines are caused by the 'missing row' surface reconstruction of the Pt(110) substrate. Normalizing to a Pt monoatomic step height of 1.4 ± 0.1 Å,[21] the apparent height of the isolated C60 molecules is roughly 6-7Å. This is consistent with widely reported C60 heights,[21] confirming that the bright dots are C60 molecules. It isn't immediately clear what is creating the smaller dots in the STM image; but their apparent height of 1-2 Å indicates that they are likely Pt adatoms (the van der Waals radius of a Pt atom is 1.75 Å[22]).

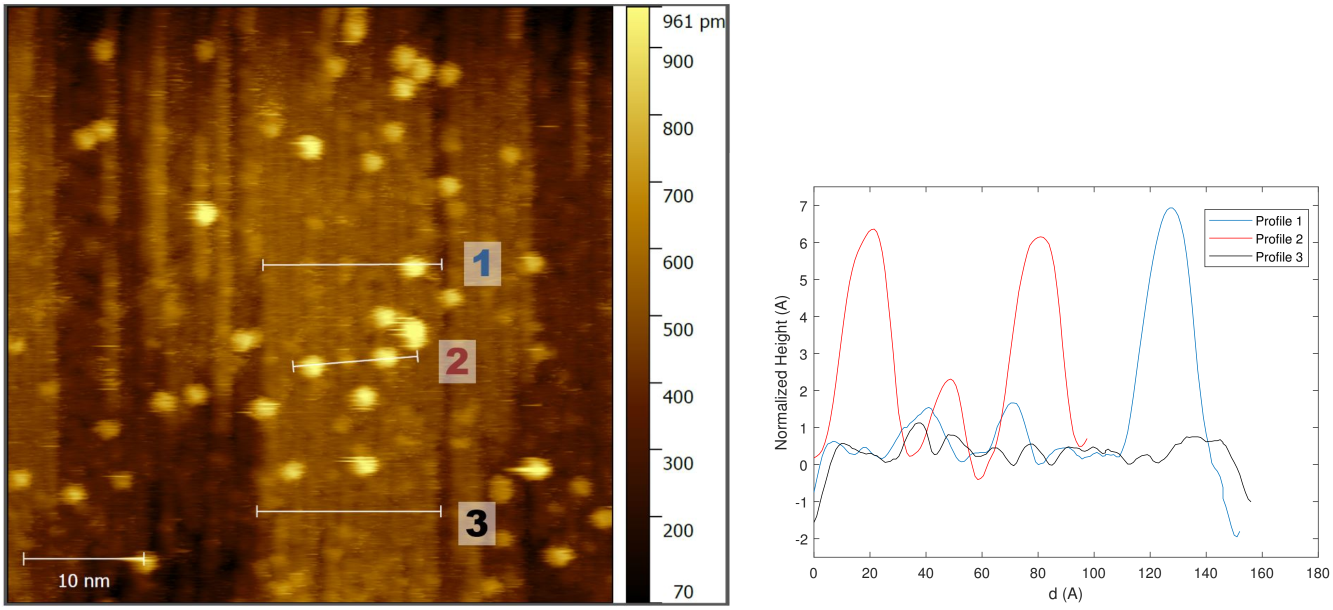

Figure 3.4: STM image (0.01 V, 0.1 nA) of a C60-decorated Pt(110) surface. Three line profiles are shown.

The resolution of the Pt(110) surface reconstruction in Figure 3.4 shows that large crystalline terraces are achievable using the sample preparation techniques described in the previous section of this work. In addition, since this image was taken over an approximately 30-minute duration, this image shows that the C60 molecules do not appreciably diffuse at room temperature over the Pt(110) surface. This is a promising first indication that Pt(110) is a suitable material to use as a bottom electrode in our molecular junction.

4 Tip Preparation

The top electrode of our proposed single-molecule junction is a sharp STM tip. In this section, I describe the procedures used to fabricate and characterize atomically sharp tungsten tips.

4.1 W Tip Preparation

Tungsten tips are fabricated by electrochemically etching a 0.1 mm tungsten wire in a 9.8 M KOH solution at 3 V_{DC}. The electrochemical reaction that takes place is shown in Equation 4.1.

$$anode : H_2O + 6e^- \rightarrow 3H_2(g) + 6OH^-$$

$$\underline{cathode : \ W(s) + 8OH^- \rightarrow WO_4^{2-} + 4H_2O + 6e^-}$$

$$W(s) + 2OH^- + 2H_2O \rightarrow WO_4^{2-} + 3H_2(g) \tag{4.1}$$

The shape of the tip is determined by two main factors. The first factor is the shape of the concave meniscus that is formed around the wire when it immersed in the electrolyte. Due to the tapered geometry of the meniscus, ion diffusion into and out of the meniscus occurs more slowly. Therefore, the reaction rate within the meniscus is slower than the reaction rate elsewhere, and the region of wire forming the meniscus is etched more slowly. The second factor that determines tip shape is a product of the electrochemical reaction at the cathode: tungstate (WO_4^{2-}). Tungstate ions have a high density, which causes them to preferentially diffuse down the tungsten wire and shield the lower region of the wire from the reaction. Therefore, the lower region of the wire is etched more slowly. Together, these two factors create a ‘necked’ shape in the tungsten wire. When the necking is so severe that the top of the wire can no longer support the weight of the bottom of the wire, the bottom section beaks off, leaving a sharp tungsten tip. Optical images of an etched tungsten tip are shown in Figure 4.5.

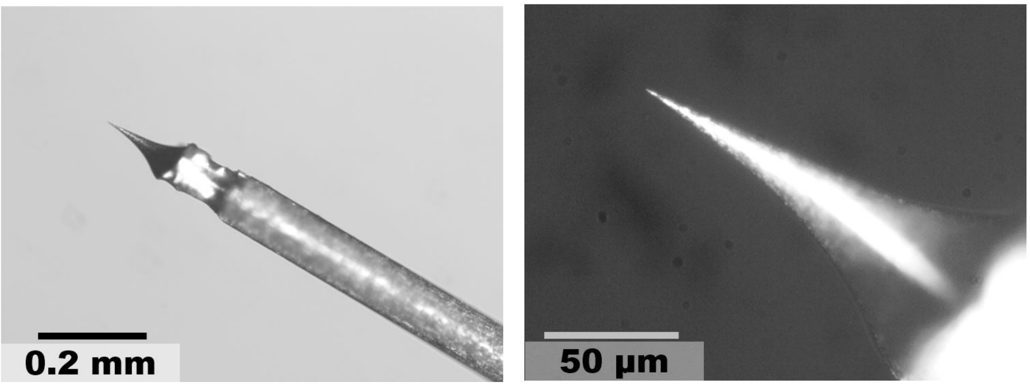

Figure 4.5: 10X (left) and 50X (right) images of an electrochemically etched tungsten tip.

Once etched, the tips are briefly annealed to approximately 500°C (a dull red glow) in vacuum. This evaporates the tip's hydration layer and sublimates surface contaminants.

4.1.1 Field Emission Microscopy

Once annealed, field emission microscopy (FEM) is used as a preliminary test of tip sharpness before the tip is transferred to the STM chamber for FIM imaging. FEM is a simple microscopy, requiring only a back electrode and a high voltage source, with a voltmeter connected in series. A high negative bias is applied to the tip, causing electrons to tunnel from the tip apex through the vacuum gap between the tip and the counter electrode. The electrons are then collected at the counter electrode, and the emission current is read with the voltmeter. This field emission effect occurs only in the presence of very high electric fields. In our case, a large electric field is supplied by the high voltage supply, and the field is further enhanced by the sharpness of the tip. This is because the electric field is locally enhanced in regions of high curvature (see Section 2.2). Therefore, the sharper the tip, the lower the bias needed to induce tunneling from the emitter to the counter electrode. A tip that is acceptably sharp for FIM produces approximately 100 nA of tunneling current with an applied bias of < 700 V, at a separation distance of approximately 1 mm.

4.2 FIM Experiments

The purpose of our FIM experiments is to determine the atomic structure of the STM tip. With our setup, achieving atomically resolved FIM images of etched tungsten tips at room temperature is routine. Figure 4.6 shows a typical FIM image of a [111]-oriented tungsten tip with atomic resolution.

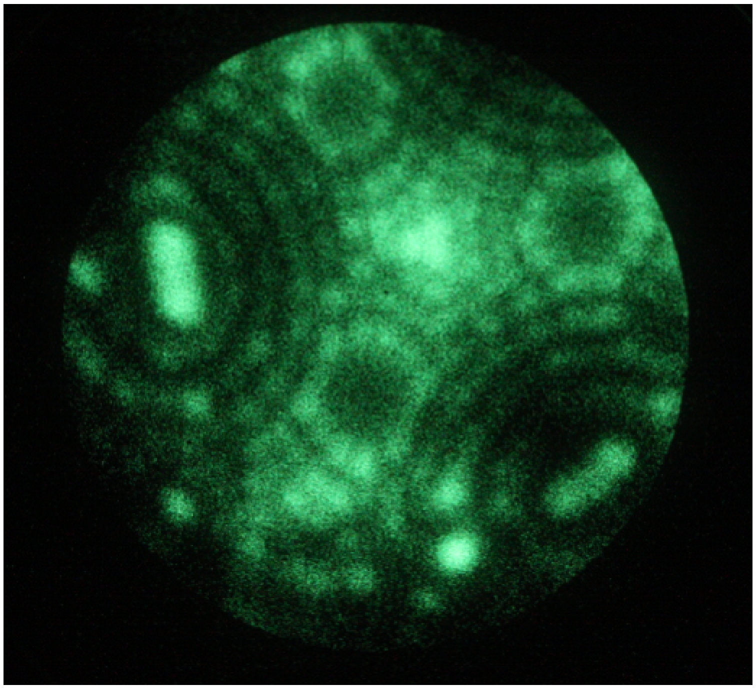

Figure 4.6: FIM image of a tip etched from a 0.13 mm (111)-oriented tungsten wire.

Deriving the xyz coordinates of the tip atoms from a FIM image, on the other hand, is not so straightforward. The main reason for this is that a FIM image is not a linear projection: the electric field lines (and therefore, the helium ion trajectories) between the tip and the planar MCP are curved. Additionally, the electric field of the tip varies over the tip surface, since the electric field depends on surface curvature. In Section 5, I describe an approach to determine the atomic coordinates of a tungsten tip corresponding to an atomically resolved FIM image.

5 Tip Model

Several different approaches have been used to study FIM and interpret FIM images. For instance, in order to understand the basic principles of FIM, and in particular, to interpret artifacts that appear in FIM images, computer simulations provide powerful insight. One common approach[23, 24, 25] involves simulating an arbitrary tip and generating its theoretical FIM image from first principles. The electric field in the region between the tip and the screen is calculated by solving Laplace's equation, and the ion trajectories are found using the classical equations of motion. This approach is useful for developing a more rigorous understanding of FIM artefacts, but it would be impossible to use this approach alone to determine the tip structure from an experimental FIM image, since the atomic tip structure must be known *a priori*.

There are two basic techniques that are routinely used to characterize experimental FIM images. First, the tip's crystallographic planes are identified by comparing a FIM image to stereographic projection maps.[15, 26] These maps give detailed information about the crystallographic structure of materials, and they are available for a variety of crystal structures and orientations because of their importance for x-ray crystallography.[27] Using these maps, the crystallographic planes are determined by inspection. Figure 5.7 shows a stereographic projection map of a [111]-oriented cubic crystal, and a corresponding FIM image.

The stereographic map in Figure 5.7(a) is found by first centering a Wulff net on a point indicating a (111) plane (purple). The (011) plane is then located by using the Wulff net to travel 35.3° (the angle between the (111) and (011) poles, see Appendix B) in one direction. The (110) and (101) planes are then easily located, given that the {110} planes are trigonally symmetric (i.e. separated by an angle of 120°) about (111) (this is known from the [111] unit cell, shown in Figure 5.12(a)). Then, the {112} planes are located: Since the angle between the {112} and {110} planes is 30°, the (121) plane is located at an angle 30° above the (011) plane. The Wulff net is then used to travel 19.5° (the separation angle between the (111) and {112} planes) in this direction.

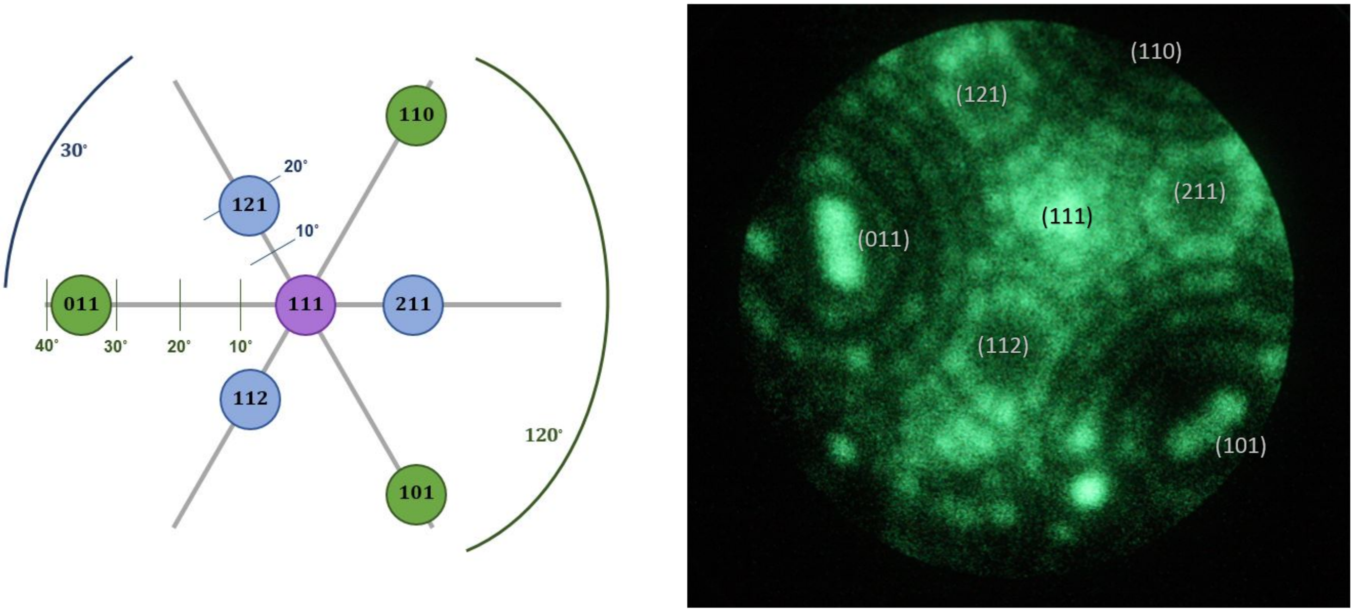

Figure 5.7: L: Stereographic projection map of a [111]-oriented cubic crystal. The 110 planes are trigonally symmetric, so they are separated by an angle of 120°, and the 112 planes are separated by 30° from the 110 planes. The 110 and 112 planes are located 35.3° and 19.5° from the (111) plane, and these angles are found using a Wulff net. R: FIM image of a tip etched from a 0.13 mm [111]-oriented tungsten wire. The {111}, {211}, and {110} planes are indicated.

The mesoscopic tip radius is then approximated using the 'ring-counting method'.[15, 28] In this method, illustrated in Figure 5.8, the local radius of curvature of the tip is approximated by counting the number of atomic steps between the top of two crystallographic planes. Using this approach, the tip radius r can be approximated as:

$$r = \frac{ns}{1 - cos\theta} \tag{5.1}$$

where s is the atomic step height, n is the number of single-step rings, and θ is the angle between the two poles.

Stereographic mapping and ring-counting are useful tools for interpreting experimental FIM images, but they cannot be used exclusively to determine the atomic structure (that is, the xyz coordinates of the tip atoms). In this section, I describe a new technique for finding the atomic coordinates of an experimental tip from an atomically defined FIM image.

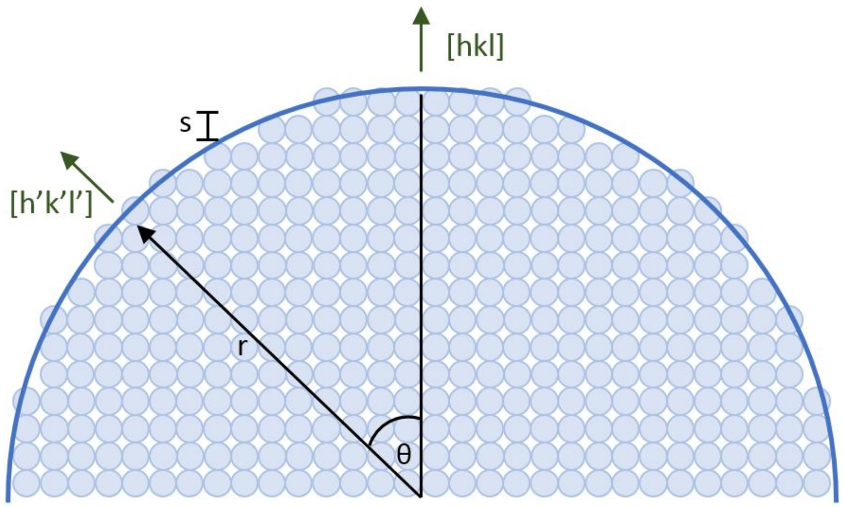

Figure 5.8: Illustration of the ring-counting method. The radius of curvature r is approximated by counting the number of steps (with height s) between the tops of two planes $[hkl]$ and $[h'k'l']$ separated by an angle θ.

5.1 The Spherical Tip

The purpose of this work is to find the coordinates of a tip which reproduces all of the features of an experimental FIM image. In 1962, Moore approximated emitters as ideal, spherical surfaces.[29] But why did he determine that this was a good approximation? Figure 5.9 shows why the spherical tip approximation is a good one. Figure 5.9(a) shows a projection of a pyramidal emitter, formed by three (211) planes terminating in a trimer apex. This tip projection is clearly a poor approximation of the FIM image shown in Figure 4.6. Figure 5.9(b), on the other hand, which shows the linear projection of a spherical tip, gives a much better approximation of the FIM image, since it reproduces many of the FIM image features.

In this section, I describe an approach to systematically generate every spherical emitter that can be formed from a [111]-oriented BCC lattice. Then, in Section 5.3, I use quantitative criteria to select the best approximations of the experimental FIM image shown in Figure 4.6.

First, the xyz coordinates of a [100]-oriented W crystal (i.e. BCC structure) are generated using Matlab. The crystal is then oriented such that the [111] direction is parallel to the

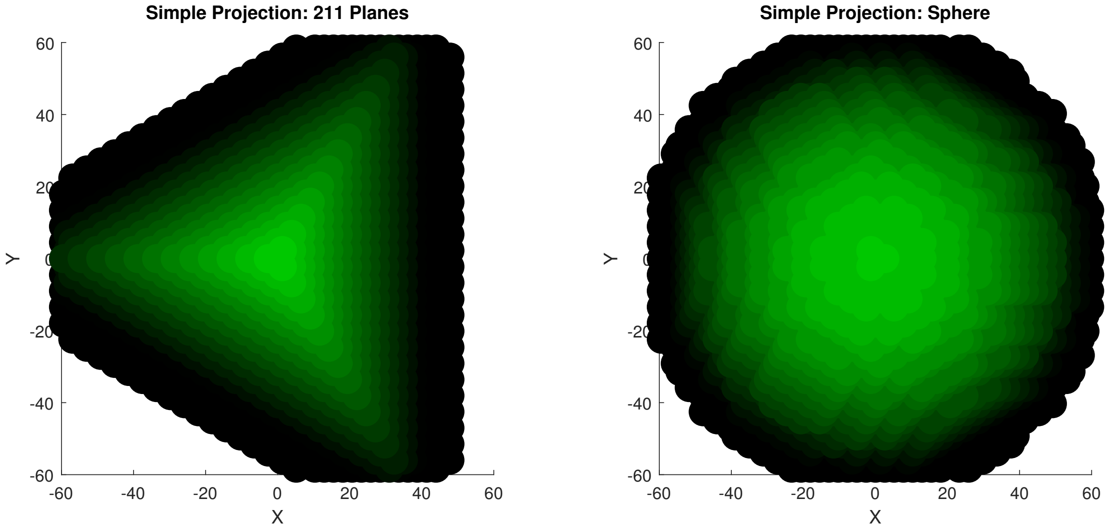

Figure 5.9: L: Projection of a [111]-oriented tip with three (211) planes terminating in a trimer apex. R: Stereographic projection of a sphere made up of hard balls.

z-axis, by rotating 45° in the x-direction and $\sim 35°$ in the y-direction (see Appendix A for derivation). Next, the crystal is cut into a sphere by removing atoms that fall outside some variable radius r. Any sphere has two features: a radius and an origin. In the following sections, I discuss how to find the radius phase space (Section 5.1.1) and where to define the origin (Section 5.1.2).

5.1.1 Finding the Radius Phase Space

In order to generate every possible spherical tip, the sphere radius must be varied. Which sphere radii are necessary to generate all possible spherical tips without redundancy? Since a lattice is composed of discrete points, it is intuitively obvious that there are not infinite distinct radii; but rather, there is a finite, predictable number of unique spheres which can be generated from a discrete lattice.

To illustrate this point, it is first necessary to clarify a physically relevant definition of 'radius'. Here, I define 'true radius' to be the distance from the origin (sphere centre) to the centroid of the furthest atom from the origin. This is distinct from the 'set radius', which is the variable radius r used to cut the crystal into a spherical shape (by keeping atoms inside r

and removing atoms outside r). Figure 5.10 illustrates the distinction between a 'set radius' and a 'true radius'. Here, the blue points show an arbitrary 2D cubic lattice. If a circle's set radius is a value for which lattice points lie on the circle (ex/ the red and yellow circles), the set radius and true radius are equal. However, if no lattice points fall on the set radius circle (ex/ the purple circle), then the set radius and true radius are not equal.

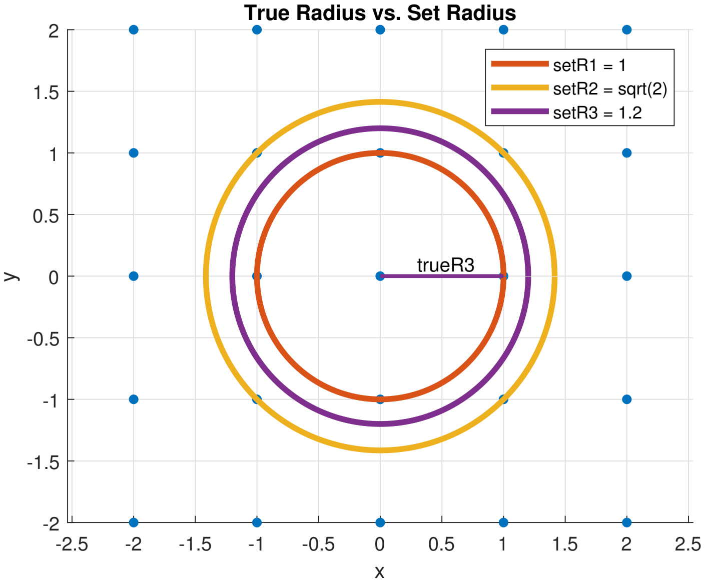

Figure 5.10: Clarifying 'Set Radius' vs. 'True Radius'. The blue points show a simple cubic 2D lattice, and the coloured circles show planes of various 'set radii'. For the yellow and red circles, the 'set radius' and 'true radius' are equal.

In order to find every non-degenerate set radius, therefore, one must simply find all of the unique distances from the sphere origin to every other point in the lattice. In the 2D example shown in Figure 5.10, the unique distances from the origin are 1 (with four-fold degeneracy), $\sqrt{2}$ (with four-fold degeneracy), 2 (with four-fold degeneracy), etc. So, to generate every possible circular plane on this 2D lattice without redundancy, only set radii of 1, $\sqrt{2}$, 2, etc. need to be included.

Every unique true radius for a 3D BCC lattice can be similarly found by calculating all of the unique distances from the origin to every other atom in the lattice. The set radii I use in this work are the true radii rounded up to the decimal place that is one order of magnitude smaller than the minimum true radii separation.

5.1.2 Defining the Origin

The second characteristic of a sphere is its origin. The origin should be placed at a symmetric site, since experimental FIM images (see Figure 4.6) show symmetry. Figure 5.11 shows an example of a tip centered at an atomic site, compared to tip of the same radius but with a horizontally translated origin. The asymmetrical origin location leads to a physically observable asymmetry in the mesoscopic structure.

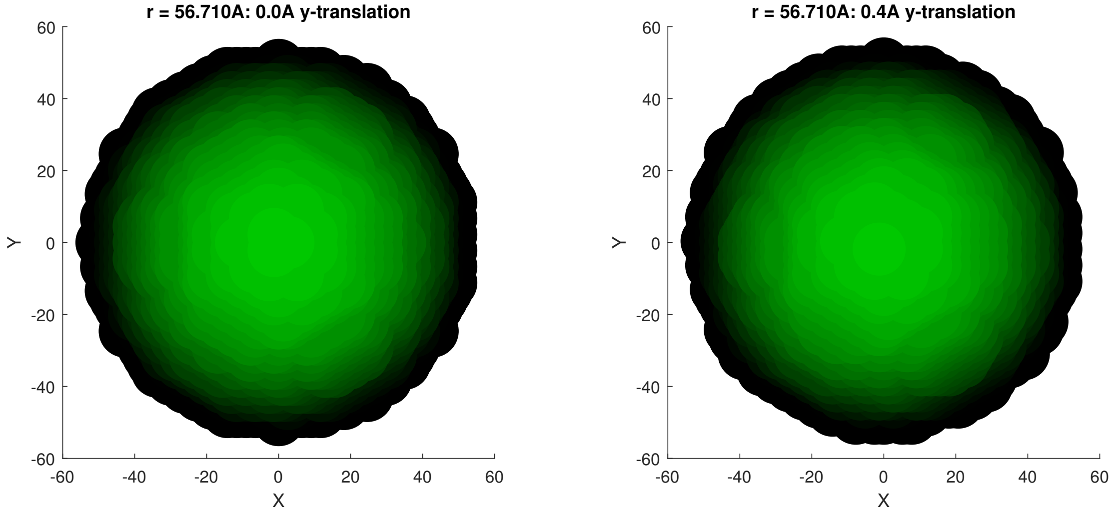

Figure 5.11: Symmetric (left) vs. asymmetric (right) tip. The symmetric tip has an origin at a symmetric location (an atom site); the asymmetric tip does not.

A [111]-oriented cubic crystal, shown in Figure 5.12, has trigonal symmetry. Its symmetry axis is a line perpendicular to the (111) plane which falls through an atom site. Figure 5.12(b) shows the symmetric [111]-oriented lattice sites: at an atom (green), at a (vacant) location in the plane directly above an atom (yellow), and directly below an atom (red). The in-plane points directly above and below the atom are inequivalent due to the ABCABC packing structure of the crystal. The origin, which must have symmetry in the x- and y-directions, must therefore fall somewhere on the line formed by these three points.

Since the set sphere curvature determines which atoms are kept and which are eliminated, the number of non-degenerate origin sites varies with the radius. Figure 5.13 illustrates this concept in two dimensions. A 2D BCC lattice is shown in blue, and circles of variable

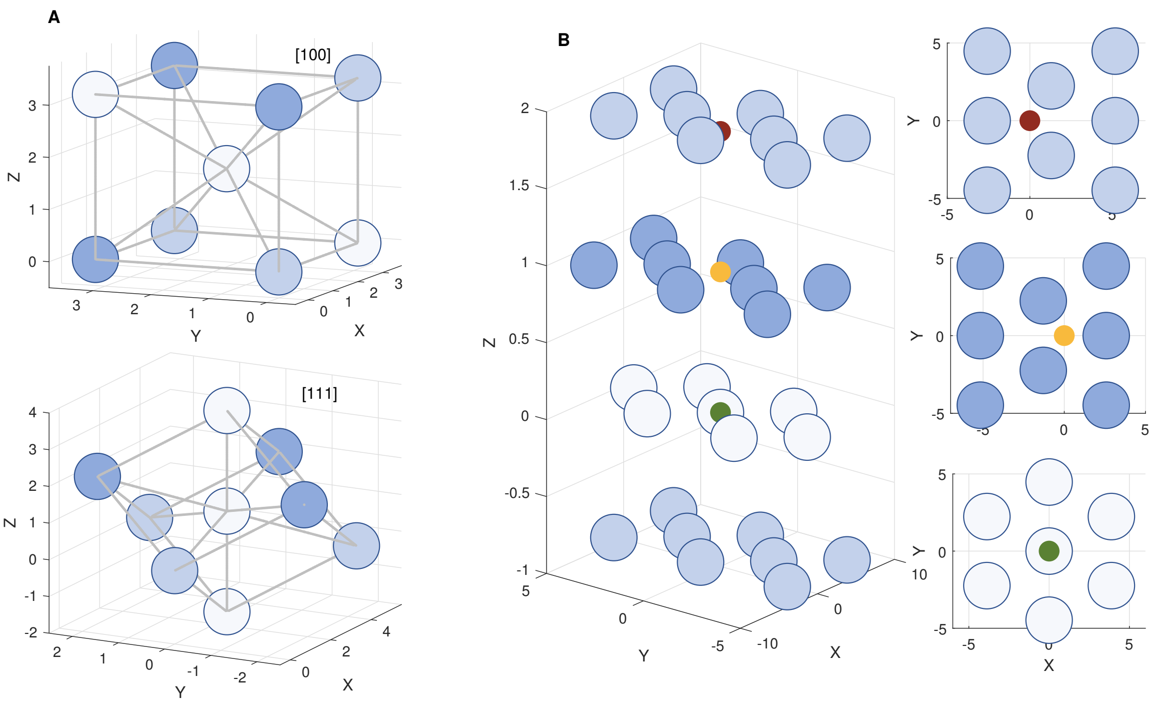

Figure 5.12: Finding the symmetry axis of a [111]-oriented BCC crystal. Figure A_{top} shows a [100]-oriented BCC unit cell, and Figure A_{bottom} shows the [111]-oriented unit cell, with different colours corresponding to different (111) planes. These planes are also shown in the lattice (Figure B_{left}). Figure B shows the three symmetric sites: at an atom site (green), at a vacancy directly above an atom (yellow) and at a vacancy directly below an atom (red).

radii are shown. Figure 5.13 shows that every non-degenerate origin site may be found by translating the circle vertically for a translation height of [0,d), where d is the distance between equivalent planes (in Figure 5.13, there are two inequivalent planes separated by a z-distance of 0.5, so d=1). Whenever the circle intersects an atom, a new structure is formed. For example, when $r = 1$ (Figure 5.13, left), the circle intersects atoms twice as the origin is translated vertically, so there are two non-degenerate origin locations: at $z = 0$ (green) and $z = \frac{a}{2} - r + \sqrt{r^2 - (\frac{a}{2})^2}$ (yellow). For $r = \sqrt{2}$, there are three non-degenerate origin sites. Furthermore, degenerate radii have the same unique origins. In the 2D case shown in Figure 5.13, this means that every possible circle with true radius [1,$\sqrt{2}$) may be drawn by setting the origin at a position $z = 0$ or $z = \frac{a}{2} - r + \sqrt{r^2 - (\frac{a}{2})^2}$. This is shown in the rightmost subfigure in Figure 5.13. The green and yellow circles for $r = 1.2$ produce structures that are identical to the structures created by the green and yellow circles for $r = 1$. The black circle is located at an arbitrary location, and shows a structure that is degenerate to the green circle structure.

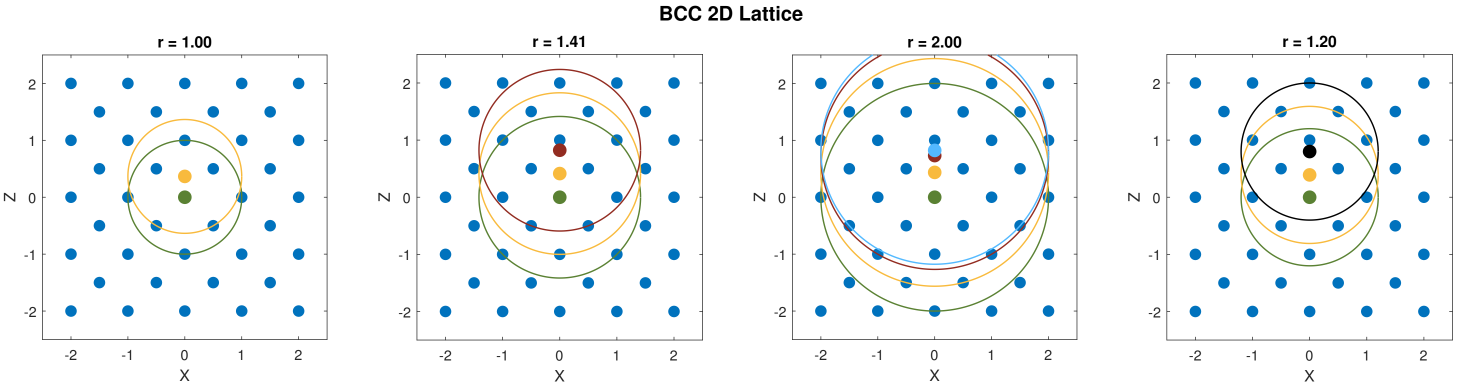

Figure 5.13: Drawing set circles (radii = $1, \sqrt{2}$, 2, and 1.2) with variable origins on a 2D BCC lattice (a = 1). Non-degenerate origin positions (coloured) occur wherever the circle intersects an atom as it is translated vertically. The rightmost (r = 1.2) green and yellow set circles produce structures identical to the leftmost (r = 1) green and yellow set circles. The black circle, located at an arbitrary symmetric location, shows an origin location that is degenerate to the green origin.

Similarly, non-degenerate origin sites for a 3D [111]-oriented BCC lattice are found by vertically translating the sphere from [0,r). Wherever the sphere intersects an atom, a new origin is found.

Since the 3D [111] BCC lattice is rotationally symmetric about $\hat{z}$ at any origin site, the 3D problem can be reduced to a 2D problem by eliminating equivalent points in the lattice. Figure 5.14 shows the 2D representation of the 3D [111]-oriented BCC lattice shown in Figure 5.12. For every atom, the lattice is rotated about $\hat{z}$ until that atom falls in the x-z plane (x≥0). This is not a necessary step for this model, but it does greatly reduce computation time for finding the origin and radius phase space by eliminating equivalent atoms.

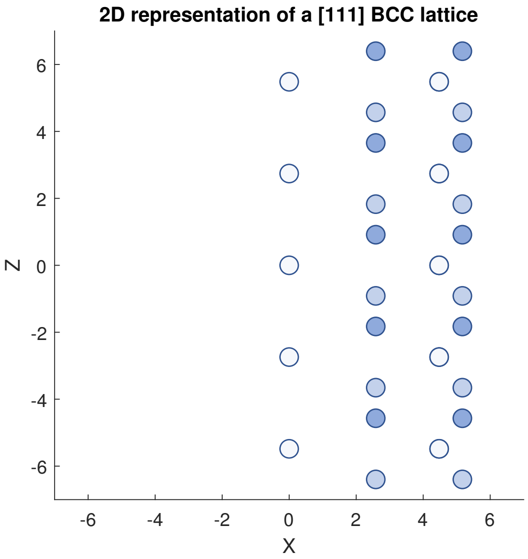

Figure 5.14: 2D representation of a 3D [111] BCC lattice, with equivalent points removed.

5.2 F-d Curves

In this section, I use a simple model to explore the basic properties of spherical [111]-oriented tungsten tips. In particular, I am looking to answer the question: 'Does the *atomic* configuration of the tip or the *mesoscopic* radius play a larger role in tip-sample interactions?' If the mesoscopic radius plays the larger role, then a 62.038 Å tip could potentially be approximated as a 62 Å tip, or even a 60 Å tip.

To test this, I use the Lennard-Jones model to determine how each spherical tip interacts with a point-particle. The Lennard Jones model, shown in equations 5.2 and 5.3, is a simple model which describes the long-range van der Waals attraction (r^{-6}) and short-range Pauli repulsion (r^{-12}) between two interacting particles.

$$U(r) = 4\epsilon \left[\left(\frac{\sigma}{r}\right)^{12} - \left(\frac{\sigma}{r}\right)^{6} \right] \tag{5.2}$$

$$F(r) = -48\frac{\epsilon}{\sigma} \left[\left(\frac{\sigma}{r}\right)^{13} - \left(\frac{\sigma}{r}\right)^{7} \right] \tag{5.3}$$

Figure 5.15 shows the Lennard-Jones interaction between an arbitrary tip (green, inset) and a point-particle sample (grey, inset), where $\sigma \approx 2.2381$ Å, the distance between atoms within a (111) tungsten plane. The Lennard-Jones parameters quantify the main features of the interaction: $\mathrm{r_o}$ is the tip-sample separation distance at which $\mathrm{U} = 0$, $\mathrm{r_e}$ is the distance where $\mathrm{U} = \mathrm{U_{min}}$ ($\mathrm{F} = 0$), and $\mathrm{r_s}$ is the distance where $\mathrm{F} = \mathrm{F_{max}}$.

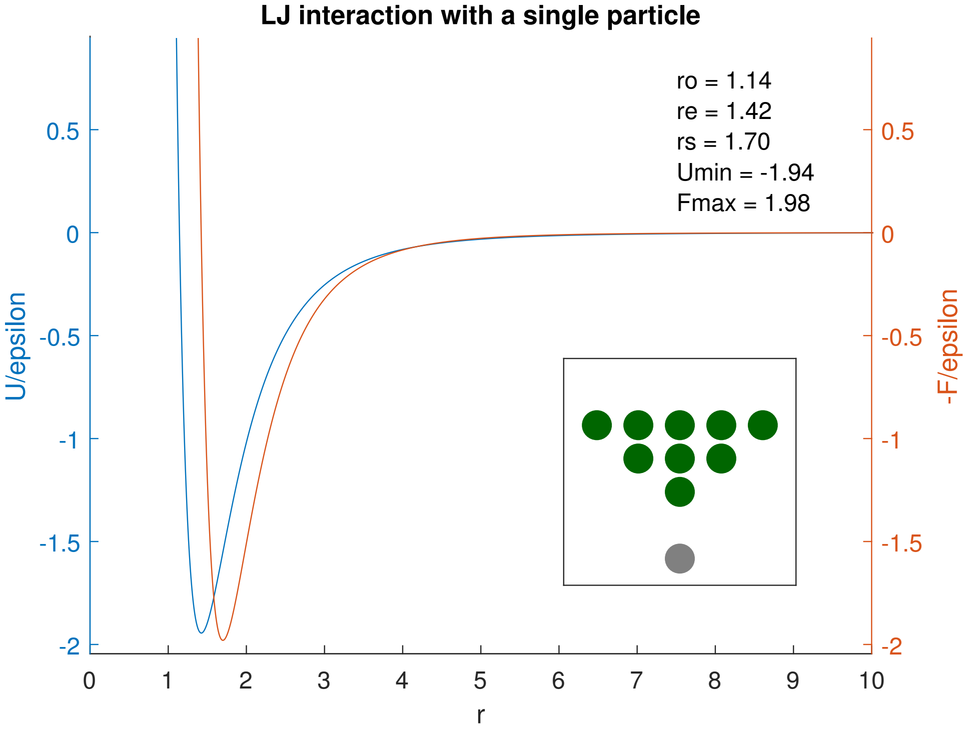

Figure 5.15: The Lennard-Jones interaction between a tip (green) and a point-particle sample (grey). The Lennard Jones parameter values are shown in the top-right corner.

From Figure 5.15, we can see that the interaction potential falls to 0 when the tip-sample separation distance is greater than approximately 5 Å. This means that tip layers higher than the $\sim 5^{\text{th}}$ layer have a negligible effect on the interaction. Therefore, smaller tips can be directly compared to larger tips, without any additional effects due to more atoms coming into play.

Figure 5.16, which gives the Lennard-Jones parameters for spherical tips with a radius between 0 and 120 Å, shows that there are three distinct categories of interaction between the tips and the point-particle. The reason for this is that the (111) BCC planes have a unique structure: the distance between planes (~ 0.9137 Å), and even the distance between two planes ($\sim 0.9137\times 2$ Å), is smaller than the distance between atoms within a plane (~ 2.2381 Å). Therefore, for a point-particle sample centered at $x, y = 0$, the strongest interaction does not necessarily come from the plane that is closest to the sample: rather, it comes from the plane which contains the $x, y = 0$ atom.

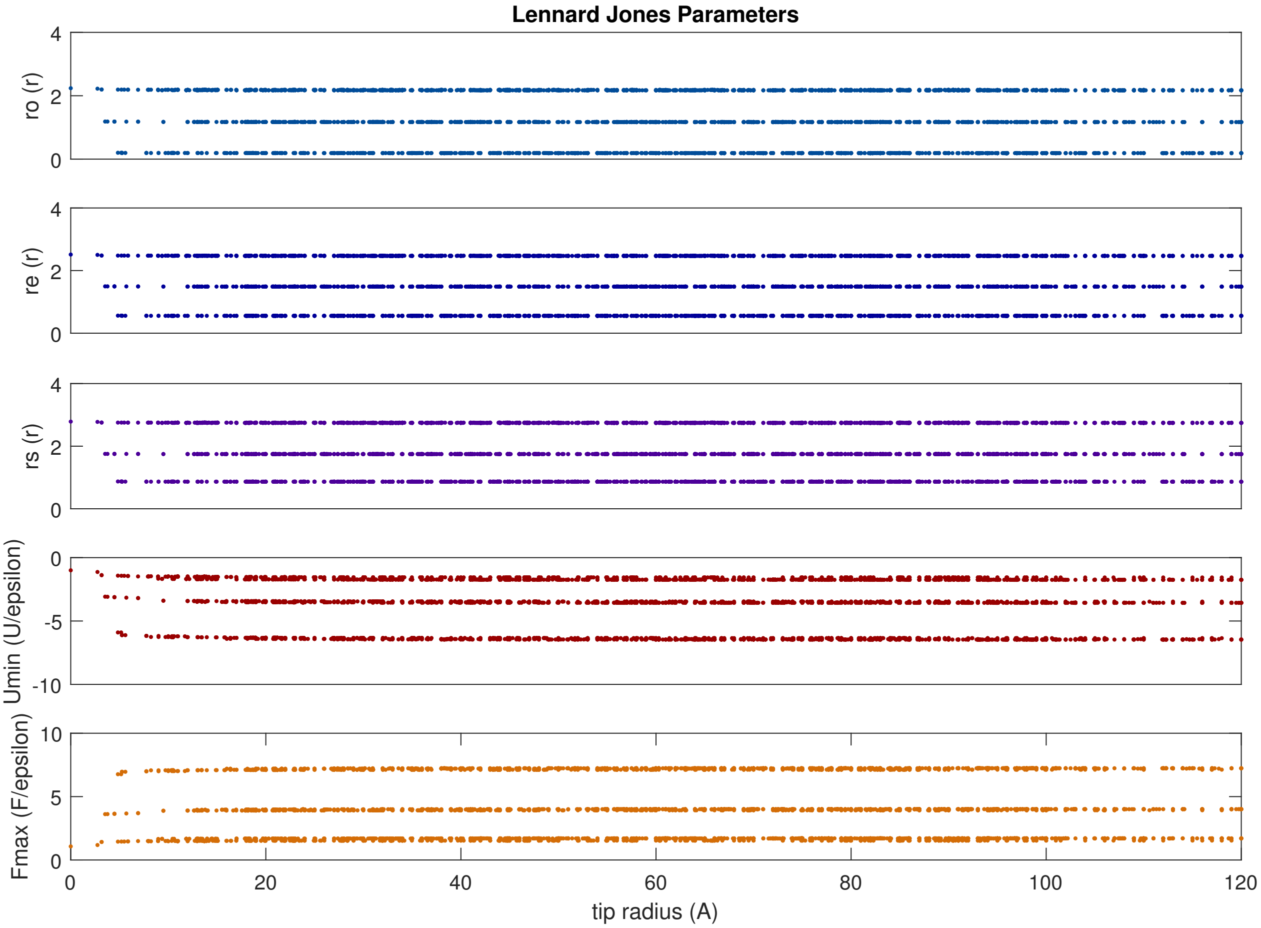

Figure 5.16: Lennard Jones parameters of every possible spherical tip with a radius between 0 and 120 Å interacting with a point particle.

Recall that the packing structure of a [111]-oriented BCC crystal is ABCABC, shown in Figure 5.12. The consequence of this ABCABC structure is that are three possible locations for the $x, y = 0$ atom. If the lowest plane is the lightest blue plane shown in Figure 5.12(b), then the $x, y = 0$ atom is in the first plane ($z = 0$). If the medium-blue plane is the lowest plane, then the $x, y = 0$ atom is in the second plane ($z \sim 0.9137$ Å). If the darkest blue plane is the lowest plane, then the $x, y = 0$ atom is in the third plane ($z \sim 0.9137 \times 2$ Å). Therefore, the three different 'types' of tip interaction which we observe in Figure 5.16 arise due to this ABCABC stacking structure.

In this model, the sample was a point-particle, which is a poor model of most real-world samples. However, the point-particle is not unlike many features that do arise in surface science: adatoms, for example, as well as step edges and – of particular relevance for this thesis – single molecules. Therefore, even this simple model suggests that the *atomic* tip structure plays a highly important role in single-molecule SPM experiments.

5.3 Narrowing Down the Tip Structures

So far, I have developed a strategy for finding every possible spherical [111]-oriented tungsten tip. In total, for a radius between 0 and 120 Å, there are 4936 non-degenerate spherical tip structures. Now, we must narrow down these possibilities to find the best approximations of the experimental tip.

FIM images have distorted distances and local magnifications, so the simplest, most reliable way to compare the model tips with the FIM image is to count the number of atoms or the number of planes which define the surface features. Figure 5.17 shows how the planes between the apex and the (110) and (211) planes are countable: There are six steps between the apex and the topmost (110) plane (blue), and there are three steps between the apex and the (211) plane (yellow). Similarly, the number of atoms forming certain features can be very well-defined. For example, while the FIM image does not show how many atoms form the topmost (211) plane, it does show that at least 12 atoms form the (211) plane boundary.

Therefore, the model tips can be narrowed down based on these types of features. With only three criteria, the 4936 model tips are reduced to five possibilities: stipulating that the

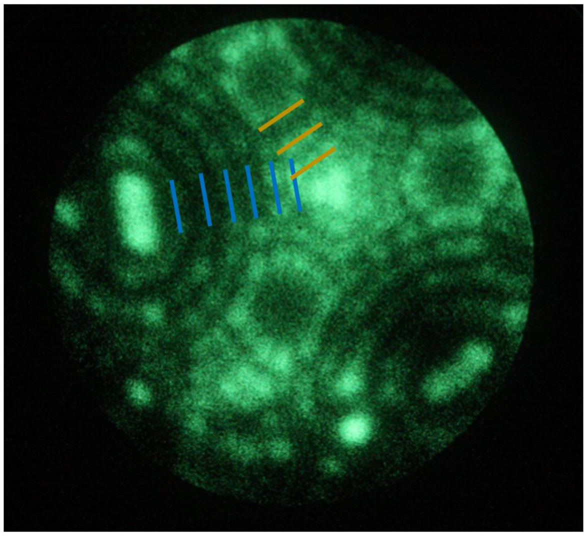

Figure 5.17: Counting the planes forming an experimental tip. There are 6 planes between the apex and the top of the (110) plane (blue), and three planes between the top and the top of the (211) plane (yellow).

tip must have 12 atoms forming the boundary of the second (111) plane reduces the number of models to 282; stipulating that the tip must have a minimum of 12 atoms forming the (211) plane boundary further reduces the number of models to 184; and finally, stipulating that the (110) plane must have between 3-5 atoms brings the grand total to five possible tip structures. These structures are shown in Figure 5.18. Some of them are much better approximations than others: Tip A and Tip B, for instance, do not satisfy the 'counting planes' criteria because they have only four intermediate steps between the apex and the (110) plane. Tip C, on the other hand, has too many steps between the apex and the (110) plane (it has seven).

Tip D and Tip E are the best approximations of the experimental tip structure shown in Figure 4.6: That is, they reproduce nearly all of the features seen in the FIM image. Like the FIM image, they have six steps between the apex and the (110) plane, three steps between the apex and the (211) plane, the point of the apex triangle points toward the (110) planes, the second and third (111) planes appear highly hexagonal, etc.

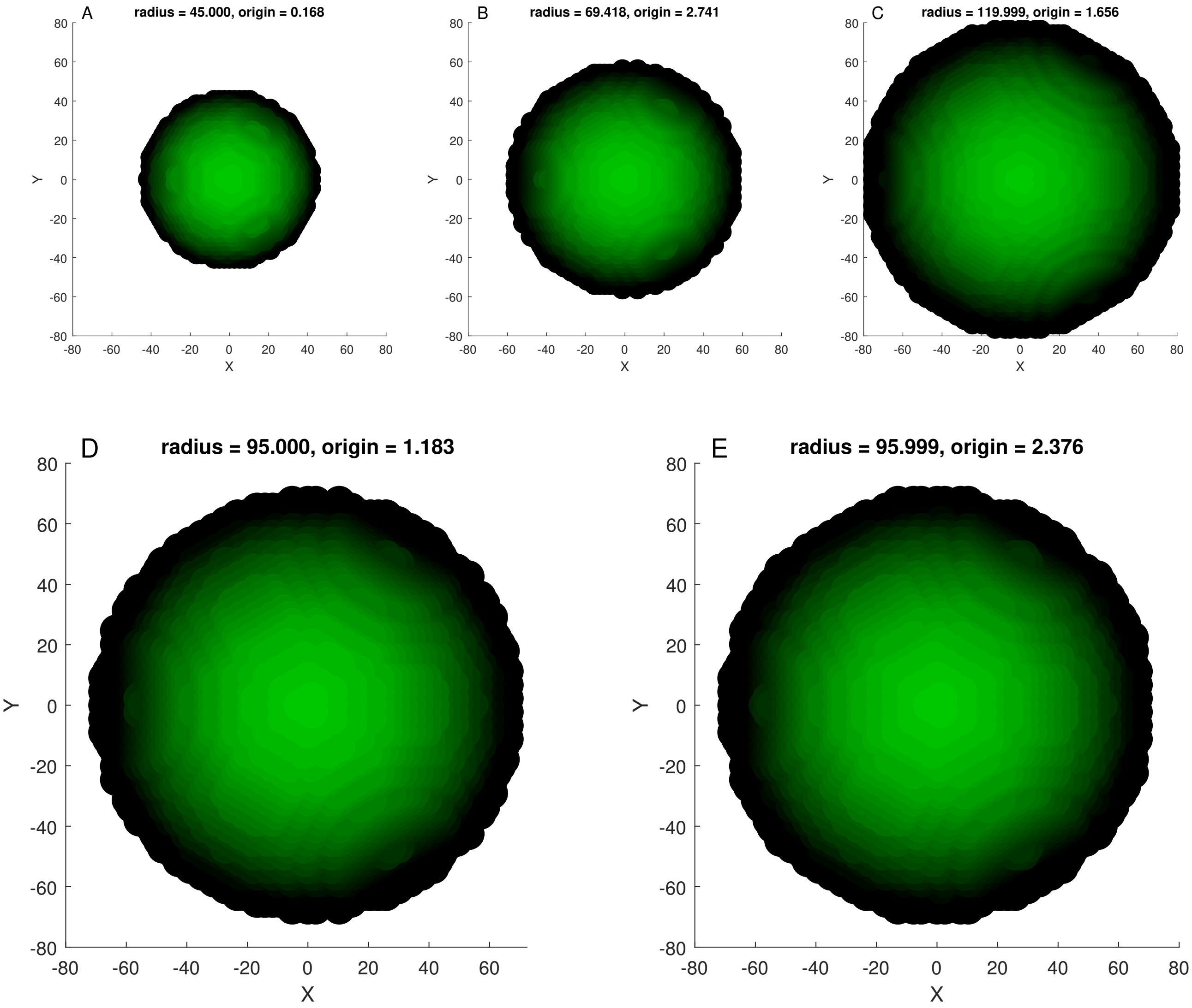

Figure 5.18: Projections of tips that meet ‘counting atoms’ criteria. Tips D and E give the best approximations of the experimental tip structure shown in Figure 4.6.

5.4 Comparison to Ring Counting

The ring-counting method, described in detail in the introduction to this section, is a common tool for approximating the mesoscopic radius of FIM-imaged SPM tips. How do the model tips, with a known radius, shown in Figure 5.18, fare with the ring-counting method?

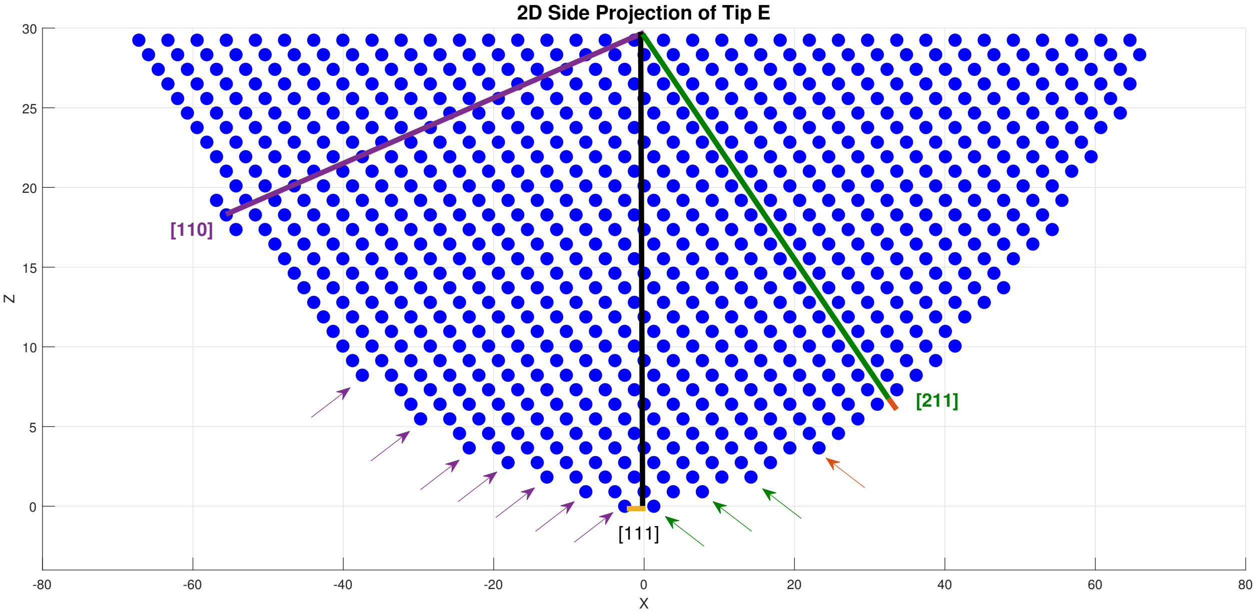

Figure 5.19: 2D projection of model Tip E in the x-z plane. The [111], [110], and [211] directions are indicated.

Figure 5.19 shows a 2D projection of Tip E, (shown in Figure 5.18(e)) in the x-z plane. The ring-counting analysis of this tip, shown in Table 5.1, clearly demonstrates some of the errors that arise with the ring-counting method. Two of these errors are discussed in an unpublished work by W. Paul and P. Grütter (2013). First, if the rings in a FIM image do not correspond to a single atomic step, the tip radius will be underestimated.[30] Second, the interplanar spacing s used in Equation 5.1 should be carefully identified.[30] If the rings *do* correspond to single atomic steps, then s should be the interplane spacing *of those steps.* For example, in Figure 5.19, each plane between the (111) and (110) poles in the [111] direction does not produce a ring in the FIM image. Therefore, it would be inaccurate to use the (111) plane spacing for interpreting the FIM image created by this tip. Rather, each of the rings (purple arrows) corresponds to a single (110) step, so the interplane spacing s that should be used is s_{110}=2.2381 Å.

However, the first line in Table 5.1 shows that even when this plane spacing is used, an inaccurate tip radius is found: The true radius is 95.999 Å, while the predicted radius is 97.4 Å. The reason for this is that the position of the final ring – the trimer apex – is not actually equivalent to the position of the (111) pole: The (111) pole falls directly in the middle of the trimer, so there is some extra distance (shown in yellow in Figure 5.19) which is unaccounted for. This shows that the number of steps n is not necessarily a whole number: Table 5.1 shows that, in the case of Tip E, n=7.8.

Tip E

	n	s (Å)	θ (°)	r (Å)
(110) to (111)	7	2.2381	35.3	**97.4**
(110) to (111)	**7.8**	2.2381	35.3	95.999
(211) to (111)	3	1.2922	19.5	**67.6**
(211) to (111)	**4.2**	1.2922	19.5	95.999

Table 5.1: Ring-counting analysis of model Tip E (r = 95.999Å), using Equation 5.1. In each case, the variable parameter is bolded. s and θ are found using the equations shown in Appendix B (s_{110}=2.2381 Å, s_{211}=1.2922 Å, θ_{110}=35.3°, θ_{211}=19.5°).

There is a final error in the ring-counting method, which is apparent from the (111) to (211) analysis of Figure 5.19. Using the ring-counting method, the number of atomic steps (in the [211] direction) between the (111) and (211) poles is n=3 (shown as green arrows in Figure 5.19). However, this leads to a grossly inaccurate radius prediction of 67.6 Å! The reason for this is that even a tip that is produced with a spherical model is *not spherical*, because it is composed of discrete points. In the case of Figure 5.19, the set radius along the [211] direction is greater than the true radius (i.e. the 95.999 Å tip radius includes the length indicated by the small orange line). Therefore, an extra step (indicated by an orange arrow) should be included in the ring-counting method.

Note that the ring-counting analysis shown in Table 5.1 also applies to the experimental tip shown in Figure 4.6, since the directions and number of planes between poles is identical. Using the ring-counting method to determine the radius of the experimental tip would lead to a radius prediction of $\frac{97.4+67.6}{2} = 82.5\pm14.9$ Å. Using the ring-counting method, then, a radius as small as 67.6 Å should be a reasonable prediction! This is not the case. Figure 5.18(b) shows a 69.4 Å tip, which is clearly much smaller than the experimental tip: There are only five planes between the (111) pole and the (110) pole, while the experimental tip has seven.

6 Conclusion

In this thesis, I described an approach to construct an atomically defined Pt(110)-C60-W junction, using a new model to find the atomic coordinates of a W tip. This model is adaptable to different tip structures, and additional features which are not represented in a spherical tip model (such as defects, adatoms, etc.) can be easily incorporated. This yields very good approximations of an experimental tip structure, meaning that they reproduce all of the features observable with FIM. Ideally, each of the best models will be tested simultaneously during theory/experiment comparisons.

Using this tip model, I demonstrate the two common ring-counting errors first identified by W. Paul and P. Grütter (2013): FIM rings must correspond to single atomic steps; and the interplanar spacing s should correspond to the spacing of those steps. I also propose two additional sources of error: A ring does not necessarily terminate at a pole (so n is not necessarily a whole number); and *no* tip is truly spherical (even tips found using a spherical model) because they are composed of discrete points. These results suggest that the ring-counting method should be used with extreme caution: In fact, the ring-counting method may be most useful as an order-of-magnitude first approximation of tip radius.

In the future, it would be fascinating to explore the theoretical transport properties of a variety of the W tip models: To date, the atomic coordinates of typical experimental W tips haven't been available to theorists, so transport simulations have often used highly simplified (often unrealistic) tips. The tip model described in Section 5 produces the atomic coordinates of realistic experimental tips, so comparisons of a selection of these tips would give an indication of how sensitive real-world STM experiments are to the atomic tip structure. This would be highly informative for both the experimental and theoretical STM community.

Finally, the natural future direction of this work is to assemble the Pt(110)-C60-W junction, and compare conductivity experiments to theoretical DFT predictions. This will lead to a sophisticated understanding of conduction properties of individual molecules, and will help pave the way toward molecular electronic devices.

APPENDICES

APPENDIX A

The [100] to [111] lattice rotation

In Section 5 of this thesis, I describe a procedure to model and characterize spherical tungsten STM tips. To do this, I first generate a [100]-oriented BCC lattice with the lattice constant of tungsten: $a = 3.1652$ Å. Then, I rotate this lattice so that it is oriented in the [111] direction.

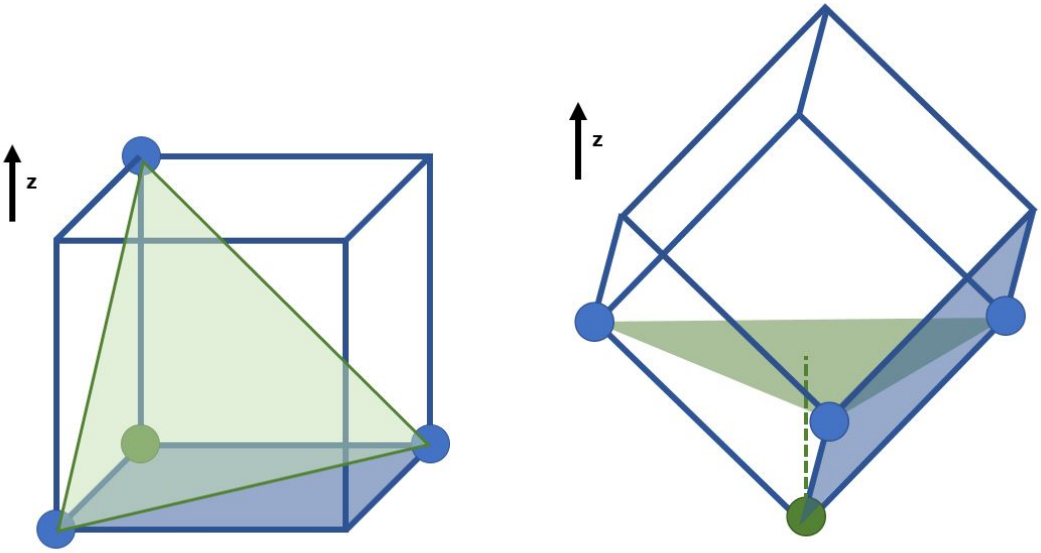

Figure A.1: Left: [100]-oriented cubic cell. Right: [111]-oriented cubic cell. Not all atoms are shown. A (100) plane is shown in blue, and a (111) plane is shown in green.

Figure A.1(a) shows a cubic unit cell, where the blue-shaded section represents a (100) plane, and the green-shaded section represents a (111) plane. The first rotation (in the x-direction) is intuitively 45°. The second rotation, in the y-direction, is found using simple trigonometry. Since the angles forming the green triangle are each 60°, the distance d to its centroid is:

$$d = L\sqrt{\frac{2}{3}}$$

where L is the unit cell length. The angle θ of rotation is:

$$\cos\theta = \frac{d}{L}$$

$$\theta = \cos^{-1}\sqrt{\frac{2}{3}} \approx 35°$$

and the corresponding rotation matrices used to rotate the crystal's xyz coordinates from a [100] orientation to a [111] orientation are therefore:

$$xRot = \begin{bmatrix} 1 & 0 & 0 \\ 0 & \sqrt{\frac{1}{2}} & -\sqrt{\frac{1}{2}} \\ 0 & \sqrt{\frac{1}{2}} & \sqrt{\frac{1}{2}} \end{bmatrix} \qquad yRot = \begin{bmatrix} \sqrt{\frac{2}{3}} & 0 & \sqrt{\frac{1}{3}} \\ 0 & 1 & 0 \\ -\sqrt{\frac{1}{3}} & 0 & \sqrt{\frac{2}{3}} \end{bmatrix} \tag{A.1}$$

APPENDIX B

Crystallography

Tungsten has a BCC crystal structure and a lattice constant of 3.1652 Å. Its geometric features (such as the angles and distances between planes) are therefore easily found using simple geometry. In this section, I provide a brief overview of the crystallography of a BCC lattice.

The angle θ between two planes A and B is found from the following relation:

$$\cos\theta = \frac{\vec{n}_{\mathrm{A}} \cdot \vec{n}_{\mathrm{B}}}{\mid \vec{n}_{\mathrm{A}} \mid\mid \vec{n}_{\mathrm{B}} \mid} \tag{B.1}$$

where $\vec{n}_{\mathrm{A}}$ and $\vec{n}_{\mathrm{B}}$ are vectors normal to the A and B planes, respectively. The angle between the (211) plane and the (111) plane is therefore:

$$\theta_{211} = \cos^{-1}\left(\frac{2\times1+1\times1+1\times1}{\sqrt{3}\sqrt{6}}\right) = \cos^{-1}\left(\frac{2\sqrt{2}}{3}\right) \approx 19.5^{\circ} \tag{B.2}$$

and similarly, the angle between the (110) plane and the (111) plane is:

$$\theta_{110} = \cos^{-1}\left(\sqrt{\frac{2}{3}}\right) \approx 35.3^{\circ} \tag{B.3}$$

In the tip model described in Section 5, these plane angles are primarily used to identify specific planes in the spherical tungsten tips (notably, for evaluating which models best represent the experimental structure).

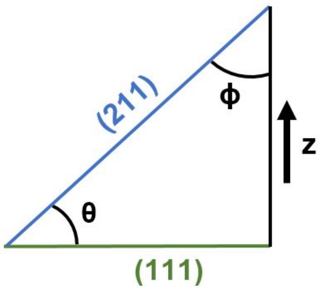

Figure B.1: Finding the angle θ between the (111) plane and the (211) plane.

The distance s between planes is:

$$s = \frac{a}{\delta\sqrt{h^2 + k^2 + l^2}} \tag{B.4}$$

where h, k, and l are the plane's Miller indices, a is the lattice constant, and δ is a factor that arises due to the BCC structure. The necessity of δ in expression B.4 can be intuitively understood from Figure B.2. Whenever a plane passes through the centre atom in the BCC unit cell (such as for plane (110)), no 'additional' planes (relative to the SC unit cell) arise due to the presence of the centre atom. Whenever a plane does not pass through the centre atom (such as for planes (100) and (111)), additional planes are created by the centre atom. Therefore, if h+k+l is even (i.e. the plane passes through the centre atom), $\delta = 1$ (i.e. identical to the SC case), and if h+k+l is odd (i.e. the plane does not pass through the centre atom), $\delta = 2$.

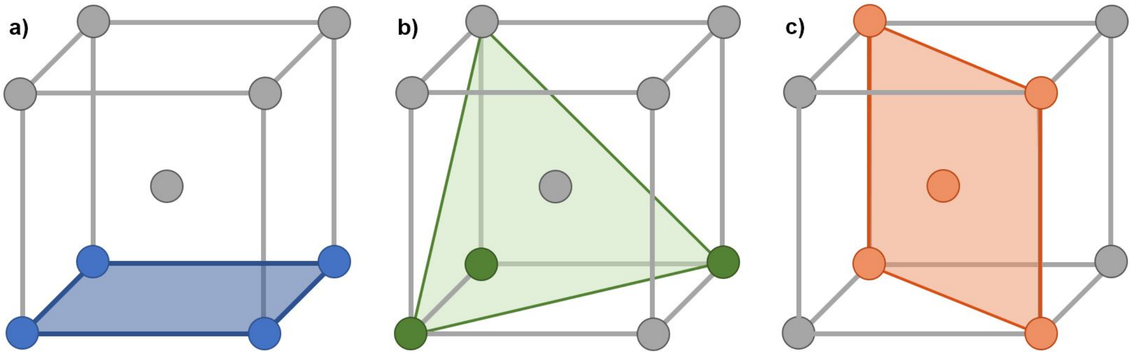

Figure B.2: 100 (a), 111 (b), and 110 (c) planes in a BCC unit cell.

APPENDIX C

Microscope Repairs

Over the duration of my time with the FIM System, several major repairs were performed. In this appendix, I will briefly discuss these repairs, and why they were needed. This is intended as advice for future FIM System operators.

My first casualty was the wobble stick in the measurement chamber. Over time, the screws attaching the two halves of the wobble stick inside the chamber had become loose, and the wobble stick snapped in two as I was attempting a routine tip transfer one otherwise beautiful Sunday afternoon. This necessitated venting, a simple replacement of the screws, and my first chamber bakeout.

During this bakeout, I heated the chamber to 200° C. This was evidently too hot, as it caused some of the glue inside the chamber to melt. The first indication that something was wrong was the stick-slip motor, shown in Figure C.1: When I finished the bake and removed the aluminum foil from the windows, I immediately noticed that the piezoelectric tube was low. When I touched it gently with the wobble stick, it fell completely out, onto the sample motor. This, of course, was catastrophic, and it merited another vent.

It was never obvious to me what had caused the piezotube slippage, since we only needed to disassemble and reassemble the stick-slip motor to get it to work again. (Thankfully, none of the piezos suffered heat damage.) I suspect that some of the glued shear stacks shifted slightly during the bake, causing the tube to fall out of place. But once the microscope was open, we saw that it needed something of an overhaul: Several other glued components had

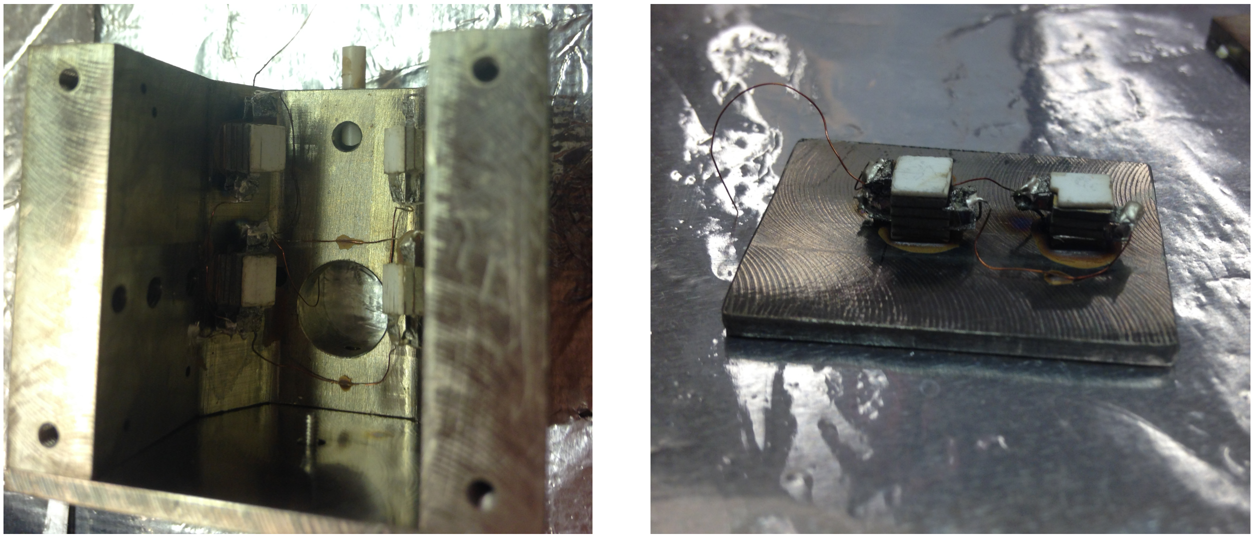

Figure C.1: Disassembled stick-slip motor, used for coarse approach.

broken, some of the pins had come loose, and the magnets holding up parts of the cage had become demagnetized. To a future FIM system operator, I would say that the first lesson I learned is: *Do not overheat during bakeouts!* (I would recommend staying well below 120° C.) On the other hand, the second lesson I learned is: If something is broken, it can always be repaired.

Next occurred an unrelated problem: I accidentally switched the laser diode and temperature controller cables, exceeding the maximum operating voltage and destroying the laser. We purchased a new laser (a QPhotonics756 nm laser, model QFLD-760-3S), but it required a new optical fibre, and so unfortunately the interferometer needed to be completely realigned. During this repair, we also implemented a new optical fibre feedthrough into UHV, designed to limit mechanical stress on the fibre (but the feedthrough is still very delicate and must be handled carefully). With the new laser, it is impossible to mistakenly switch the laser diode and temperature controller connections (as one is a female connector, the other is male), so hopefully this accident will not occur again.

Some time later, the transfer arm in the preparation chamber began to cause problems. Over time, one of the transfer arm pins had become bent, at a maximum of about 5°. It

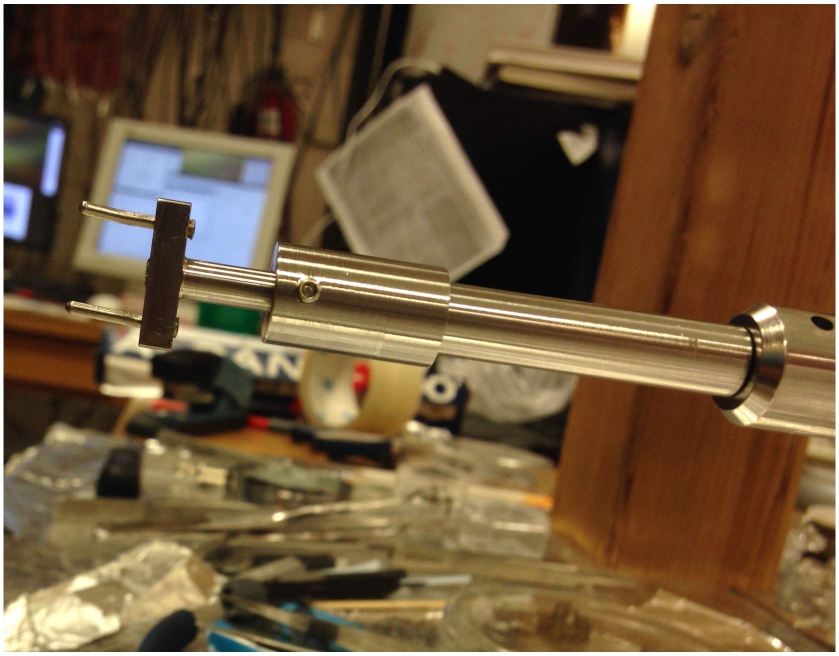

Figure C.2: Preparation chamber transfer arm. The top pin has just been straightened.

was possible to use the bent pins to transfer samples, by sliding them only ∼1/3 of the way into the sample holder, raising the transfer arm *slowly*, and immediately pushing the sample holder completely onto the pins once the transfer was complete. This was exceedingly precarious, however, and by the third time I dropped a sample I had decided it merited venting the chamber. I removed the arm and gently used pliers to straighten the pin, but I didn't do too many fine adjustments for fear of breaking it (it was surprisingly pliant). The straightened pin is shown in Figure C.2.

The next small incident involved the tip annealing stage in the preparation chamber. This didn't require venting, but I will include it here because it had me puzzled for a few days: When I attempted tip annealing, the tip did not glow (suggesting that the tip annealing circuit was interrupted). I noticed that one of the inlet leads was contacting the aluminum foil outside the chamber, shorting the circuit to ground, but removing the compromising foil did not solve the problem. In the end, the real culprit was poor contact between the tip holder and the stage pins, which I realized by testing the resistance to each side of the tip holder using the transfer arm and a multimeter. The most practical solution I came up with was to nudge the tip holder slightly with the transfer arm to improve contact (or remove a potential oxidation layer) whenever it misbehaves.

The final problem I encountered involved the FIM setup: I was unable to take any atomically resolved FIM images. An example of one of my FIM images at this time is shown in Figure C.3(a). To diagnose the problem, I systematically evaluated every component of the microscope needed for FIM to work, shown in Table C.1:

FIM Component	**Functionality Check**
Electrical connection to tip	Wobble stick and multimeter
Functional tip HV source	Large resistor and multimeter
Functional MCP HV source	Large resistor and multimeter
Functional screen HV source	Large resistor and multimeter
Pure He inlet	Preparation chamber RGA
Low system pressure	STM gauges
MCP retracted	Visual
Tip lowered	Visual
Mirror Aligned	Visual
Annealing does not melt tip	Optical image comparison pre and post-annealing
Sharp tip post-transfer	SEM on post-FIM tip (Figure C.3)
Functional MCP	IV test and comparison to specs (30μ A for 1000 V)
Functional Phosphor	(could not directly check under vacuum)
Connection to MCP	IV test and comparison to specs (30μ A for 1000 V)
Connection to Phosphor	(could not directly check under vacuum)

Table C.1: Diagnosing FIM. The components required to take a successful FIM image (right) and their corresponding test (left).

This became an increasingly perplexing problem, as each of the components listed in Table C.1 passed its respective test: The electrical connections were all strong, the helium was pure, the tips appeared unchanged pre- and post-annealing, and they were sharp (shown in SEM images, and furthermore, some of the dim FIM images I was able to achieve, like the one shown in Figure C.3(a), hint at the atomic structure representative of low-radius tips). I concluded, therefore, that the problem was with the phosphor screen. Our MCP/phosphor assembly is bakeable to 300° C, so it is unlikely that it was damaged during my 200° C bake, but phosphor does degrade when it is exposed to air. I suspect that it degraded each time

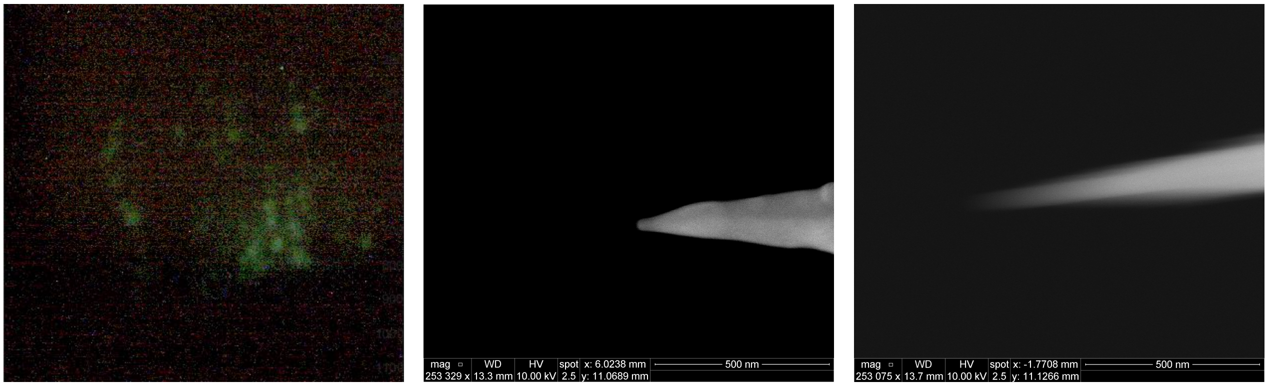

Figure C.3: (Left) Dark FIM image (with log brightness contrast). (Middle) SEM image of the tip producing the dark log image, left. (Right) SEM image of a different tip, which showed a completely black FIM image.

the chamber was vented and left open – sometimes for as long as a week – during each of the prior repairs. A new, identical phosphor screen / MCP assembly has been ordered, and will be installed once it arrives.

BIBLIOGRAPHY

[1] P.M. Agrawal, B.M. Rice, and D.L. Thompson. Predicting trends in rate parameters for self-diffusion on FCC metal surfaces. *Surf Sci*, 515:21–35, 2002.

[2] M.M. Irvine. Early digital computers at Bell telephone laboratories. *Ann Hist Comput*, 23(3):22–42, 2001.

[3] N. Singh *et al.* Ultra-Narrow silicon nanowire gate-all-around CMOS devices: Impact of diameter, channel-orientation and low temperature on device performance. *IEDM Tech Dig*, pages 1–4, 2006.

[4] V.P. Georgiev *et al.* Impact of precisely positioned dopants on the performance of an ultimate silicon nanowire transistor: A full 3-D NEGF simulation study. *IEEE T Electron Dev*, 60(3):965–971, 2013.

[5] A. Aviram and M.A. Ratner. Molecular rectifiers. *Chem Phys Lett*, 29(2):277–283, 1974.

[6] M.A. Ratner. A brief history of molecular electronics. *Nat Nanotechnol*, 8:378–381, 2013.

[7] M.A. Reed *et al.* Conductance of a molecular junction. *Science*, 278:252–253, 1997.

[8] D. Xiang *et al.* Molecular-scale electronics: From concept to function. *Chem Rev*, 116:4318–4440, 2016.

[9] S. Bouvron *et al.* Charge transport in a single molecule transistor probed by scanning tunneling microscopy. *Nanoscale*, 10:1487–1493, 2018.

[10] H. Mehrez *et al.* I-V characteristics and differential conductance fluctuations of Au nanowires. *Phys Rev B*, 65:195419, 2002.

[11] Y. Zhu *et al.* Contact, charging, and disorder effects on charge transport through a model DNA molecule. *Phys Rev B*, 69:245112, 2004.

[12] S.H. Ke. Contact atomic structure and electron transport through molecules. *J Chem Phys*, 112:074704, 2005.

[13] G. Binnig and H. Rohrer. Scanning tunneling microscope. 4343993A, 1979.

[14] J. Bardeen. Tunneling from a many-particle point of view. *Phys Rev Lett*, 6(2):57–59, 1951.

[15] T.T. Tsong. *Atom-probe field ion microscopy.* Cambridge University Press, 1990.

[16] G. Ehrlich and F.G. Hudda. Atomic view of surface self-diffusion: Tungsten on tungsten. *J Chem Phys*, 44(3):1039–1049, February 1966.

[17] A.S. Berger, D.N. Seidman, and R.W. Balluffi. A quantitative study of vacancy defects in quenched platinum by field ion microscopy and electrical resistivityI. Experimental results. *Acta Metall Mater*, 21:123–235, 1973.

[18] T.T. Tsong and J. Sweeney. Direct observation of the atomic structure of W 100 surfaces. *Solid State Commun*, 30:767–770, 1979.

[19] R. Gomer. Field emission, field ionization, and field desorption. *Surf Sci*, 299(300):129–152, 1994.

[20] Pfeiffer Vacuum Instruments. Desorption, diffusion, permeation and leaks. Retreived from www.pfeiffer-vacuum.com, [2018-02-23].

[21] T. Orzali *et al.* STM study of the initial stages of C60 adsorption on the Pt(110)-(1x2) surface. *Appl Surf Sci*, 252:5534–4437, 2006.

[22] A. Bondi. Van der Waals volumes and radii. *J Phys Chem*, 68(3):441–451, 1964.

[23] F. Vurpillot, A. Bostel, and D. Blavette. A new approach to the interpretation of atom-probe field ion microscopy images. *Ultramicroscopy*, 89:137–144, 2001.

[24] D. Niewieczeral, C. Oleksy, and A. Szczepkowicz. Image deformation in field ion microscopy of faceted crystals. *Ultramicroscopy*, 110:234–241, 2010.

[25] D. Niewieczeral, C. Oleksy, and A. Szczepkowicz. Multi-scale simulations of field ion microscopy images – Image compression with and without the tip shank. *Ultramicroscopy*, 112:1–9, 2012.

[26] A.S. Lucier. *Preparation and characterization of tungsten tips suitable for molecular electronics studies.* PhD thesis, McGill University, 2004.

[27] Y. Waseda, E. Matsubara, and K. Shinoda. *X-ray diffraction crystallography.* Springer Publishing, 2011.

[28] A.S. Lucier, H. Mortensen, Y. Sun, and P. Grutter. Determination of the atomic structure of scanning probe microscopy tungsten tips by field ion microscopy. *Phys Rev B*, 72:235420, 2005.

[29] A.J.W Moore. The structure of atomically smooth spherical surfaces. *J Phys Chem Solids*, 23:907–912, 1962.

[30] W. Paul and P. Grütter. Comment on ‘Field ion microscopy characterized tips in noncontact atomic force microscopy: Quantification of long-range force interactions’. (Unpublished), 2013.